

Universal rules for visible-light absorption in hybrid perovskite materials

Masato Kato,¹ Takemasa Fujiseki,¹ Tetsuhiko Miyadera,² Takeshi Sugita,²
Shohei Fujimoto,¹ Masato Tamakoshi,¹ Masayuki Chikamatsu,² and
Hiroyuki Fujiwara^{1,a)}

¹*Department of Electrical, Electronic and Computer Engineering, Gifu University, 1-1 Yanagido, Gifu 501-1193, Japan*

²*Research Center for Photovoltaics, National Institute of Advanced Industrial Science and Technology (AIST), Central 5, 1-1-1 Higashi, Tsukuba, Ibaraki 305-8568, Japan*

Abstract

A variety of organic-inorganic hybrid perovskites (APbX₃) consisting of mixed center cations [A = CH₃NH₃⁺, HC(NH₂)₂⁺, Cs⁺] with different PbX₃⁻ cages (X = I, Br, Cl) have been developed to realize high-efficiency solar cells. Nevertheless, clear understanding for the effects of A and X on the optical transition has been lacking. Here, we present universal rules that allow the unified interpretation of the optical absorption in various hybrid perovskites. In particular, we find that the influence of the A-site cation on the light absorption is rather significant and the absorption coefficient (α) reduces to half when CH₃NH₃⁺ is replaced with HC(NH₂)₂⁺ in the APbI₃ system. Our density functional theory (DFT) calculations reproduce all of the fine absorption features observed in HC(NH₂)₂PbI₃ and CH₃NH₃PbBr₃, allowing the unique assignment of the interband transitions in the Brillouin zone. In contrast to general understanding that the A-site cation involves weakly in the optical process, our theoretical calculations reveal that the center cation plays a critical role in the interband transition and the absorption strength in the visible region is modified by the strong A-X interaction. Furthermore, our systematic analyses show that the variation of the absorption spectrum with X can be described simply by the well-known sum rule. The universal rules established in this study explain the large reduction of α in HC(NH₂)₂PbI₃ and predict CsPbI₃ as the highest α material.

I. INTRODUCTION

Numerous organic-inorganic hybrid perovskites expressed by $APbX_3$ (A: organic cation; X: halogen atom) have been investigated¹⁻⁶⁹ in an effort to develop highly stable solar cells with high efficiencies. Although quite extensive researches have been conducted on methylammonium lead iodide ($MAPbI_3$) perovskite,^{1-44,68,69} now it becomes quite clear that the $MAPbI_3$ perovskite exhibits large instability for temperature,³⁻⁸ light illumination,⁶⁻⁹ and humidity.⁶⁻¹¹ In particular, $MAPbI_3$ shows a decomposition into PbI_2 at temperatures of ≥ 85 °C,^{4,5} which could limit the practical application of this material severely.

The thermal stability can be improved greatly when the MA cation ($CH_3NH_3^+$) of $MAPbI_3$ is replaced with a formamidinium (FA) cation [$HC(NH_2)_2^+$] having a larger molecular weight. For $FAPbI_3$, no major structural change occurs upon thermal treatment up to 150 °C.⁴⁶ However, the $FAPbI_3$ perovskite has limited long-term stability and a cubic $FAPbI_3$ crystal (α - $FAPbI_3$) shows a gradual phase transformation into a transparent δ - $FAPbI_3$ phase having a one-dimensional crystal structure.^{49,50} Such instability is caused by the larger size of FA^+ and, quite fortunately, $FAPbI_3$ -based perovskites can be stabilized by including a small amount of MA^+ and Cs^+ having smaller ionic radii.⁵¹⁻⁵⁷ The Cs addition to α - $FAPbI_3$ is also beneficial for suppressing degradation induced by humid air and light illumination.⁵³ A recent study further demonstrates the improved overall stability of α - $FAPbI_3$ by the incorporation of Cs and Br atoms.⁵⁷ Accordingly, by the optimum combination of different A-site cations and X-site halogen atoms, an ideal hybrid perovskite compound with high stability could be realized. To date, very high conversion efficiencies exceeding 20% have been demonstrated in $(FA, MA)Pb(I, Br)_3$ and $(FA, MA, Cs)Pb(I, Br)_3$ solar cells.^{52,57-59}

Nevertheless, despite the rapid progress for the solar cell fabrication, the optical process in the complex hybrid perovskite remains unclear. For the light absorption in $APbX_3$, there is a common belief that the A-site cation plays a minor role in the optical transition¹²⁻¹⁹ and only the band gap (E_g) changes slightly according to the size of the A-site cation.^{17,20} However, although many studies have been devoted to determine the dielectric functions ($\varepsilon = \varepsilon_1 - i\varepsilon_2$) of $MAPbI_3$ (Refs. 5, 23-27), $MAPbBr_3$ (Refs. 27, 63) and $MAPbCl_3$ (Ref. 27), only limited experimental results are available for the quantitative effect of the A-site cation on the light absorption.^{53,60,61} So far, the optical properties of $FAPbI_3$ (Refs. 20, 65) and $CsPbI_3$ (Refs. 65-67) perovskites have been investigated by applying density functional theory (DFT), but the influences of the A-site cation and X-site halogen atom on the absorption properties remain ambiguous.

Due to the increasing complexity of hybrid perovskite compounds, there is a pressing need for quantitative interpretation of the light absorption in various hybrid perovskites.

In this article, we establish the universal rules that define the optical effects of A and X in APbX₃ perovskite materials (A = MA⁺, FA⁺, Cs⁺; X = I, Br, Cl). In particular, we experimentally find a large variation of the absorption coefficient (α) with the A-site cation for APbI₃. Our systematic DFT calculation reveals that α of the hybrid perovskites in the visible region is determined by the quite strong interaction of the X-atom valence electron with the A-site cation. Moreover, we present that the effect of X on the perovskite dielectric function can be expressed simply by the general sum rule.⁷⁰ Based on the guiding principles established in this study, α spectra of complex hybrid perovskites at room temperature can be predicted.

II. EXPERIMENT

To determine the dielectric function of α -FAPbI₃, we prepare α -FAPbI₃ layers by a laser evaporation technique,⁵ in which PbI₂ and FAI source materials are heated by a near-infrared laser with a wavelength of 808 nm. Our earlier study on MAPbI₃ confirms that the laser evaporation method is quite helpful for the preparation of smooth hybrid perovskite layers, which are quite important for reliable optical analyses.⁵ In the laser evaporation process, the evaporation rates of the source materials are controlled by adjusting the laser power. The resulting deposition rate of FAPbI₃ layers is 2.3 nm/min. The laser evaporation process is conducted without substrate heating at a pressure of 4×10^{-4} Pa.

We find that α -FAPbI₃ and δ -FAPbI₃ layers can be formed separately by choosing proper substrates. For the preparation of α -FAPbI₃, we employ crystalline Si (*c*-Si) substrates covered with native oxides. For the deposition of α -FAPbI₃, we particularly use uncleaned SiO₂/*c*-Si substrates, as ultrasonic cleaning of the substrates using organic solvents tends to enhance the PbI₂ formation. The spectroscopic ellipsometry (SE) analyses of the cleaned and uncleaned substrates show that the thickness of an organic overlayer on the uncleaned substrate is ~ 1 Å. On the other hand, δ -FAPbI₃ can be formed by using substrates in which thin PCDTBT (poly[*N*-9''-hepta-decanyl-2,7-carbazole-alt-5,5-(4',7'-di-2-thienyl-2',1',3'-benzothiadiazole)]) layers (~ 5 nm) are formed on ZnO-coated *c*-Si substrates. The ZnO layer (50 nm) is provided to improve the adhesion of the PCDTBT layer on the substrate.

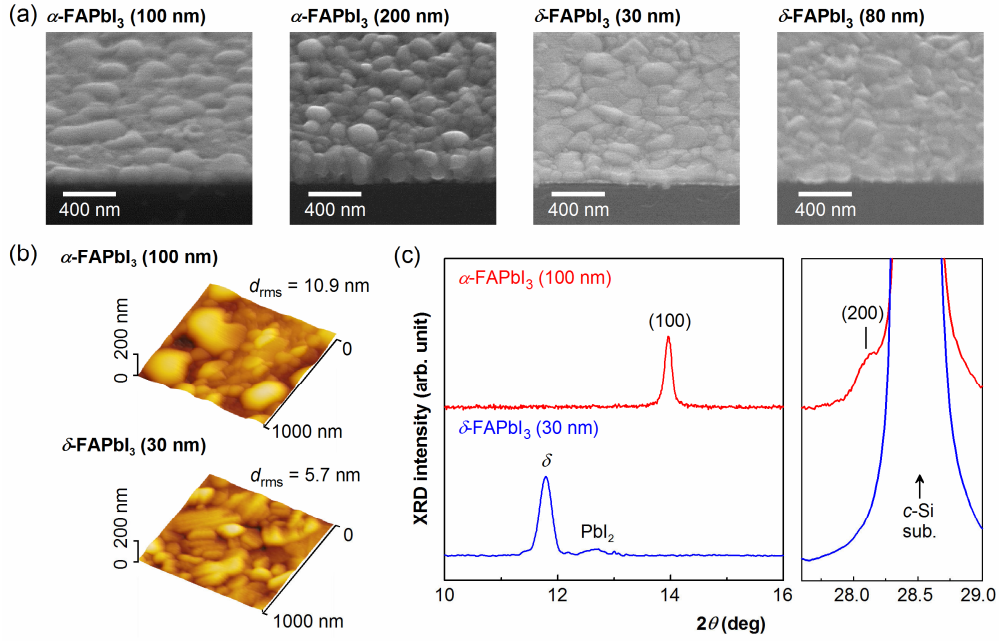


FIG. 1. (a) SEM images, (b) AFM images and (c) XRD spectra of the α -FAPbI₃ and δ -FAPbI₃ layers with different thicknesses, fabricated by the laser evaporation. The α -FAPbI₃ and δ -FAPbI₃ layers are prepared separately by using SiO₂(2 nm)/c-Si and PCDTBT(5 nm)/ZnO (50 nm)/c-Si substrates, respectively. In (b), the root-mean-square roughness (d_{rms}) obtained from each AFM image is also indicated.

Figure 1 shows (a) scanning electron microscope (SEM) images, (b) atomic force microscope (AFM) images and (c) x-ray diffraction (XRD) spectra of the α -FAPbI₃ and δ -FAPbI₃ layers prepared on the SiO₂/c-Si and PCDTBT/ZnO/c-Si substrates, respectively. The SEM images in Fig. 1(a) show significant surface roughening with increasing α -FAPbI₃ layer thickness from 100 to 200 nm, and the preparation of smooth surface is more difficult for α -FAPbI₃, compared with MAPbI₃. In fact, the root-mean-square roughness (d_{rms}) of the thin α -FAPbI₃ layer (100 nm) estimated by AFM is relatively large [$d_{\text{rms}} = 10.9$ nm in Fig. 1(b)] when compared with $d_{\text{rms}} = 4.6$ nm observed for a laser-evaporated MAPbI₃ layer.⁵ In the thick α -FAPbI₃ layer (200 nm), d_{rms} increases further to 12.6 nm.

The XRD spectrum obtained from the thin α -FAPbI₃ layer [Fig. 1(c)] shows the sharp peaks attributed to (100) and (200) diffractions of the cubic α phase.⁵⁰ On the other hand, the δ -FAPbI₃ layer with a thickness of 30 nm in Fig. 1(a) exhibits diffraction peaks at 11.8° and 12.7° due to the formation of δ -FAPbI₃ (Refs. 3, 45, 48) and PbI₂ (Ref. 11), respectively [Fig. 1(c)]. The XRD result of Fig. 1(c) confirms that, in the α -FAPbI₃ layer, the generation of the δ -FAPbI₃ and PbI₂ secondary phases is negligible.

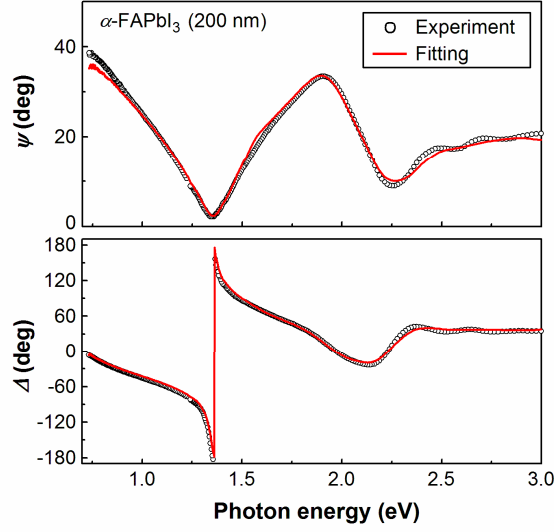


FIG. 2. (ψ, Δ) ellipsometry spectra obtained from the α -FAPbI₃ (200 nm)/SiO₂ (2 nm)/*c*-Si structure (open circles) and the fitting result calculated using the α -FAPbI₃ dielectric function extracted from the thinner layer of 100 nm (solid lines).

III. SE ANALYSIS

The dielectric functions of the α -FAPbI₃ and δ -FAPbI₃ samples are determined by SE. The SE measurements of the FAPbI₃ layers are performed in a N₂ ambient without exposing the samples to air by a procedure established earlier,⁵ as α -FAPbI₃ exhibits significant degradation in humid air.^{3,46,53,55} The SE measurements are implemented at an angle of incidence of 75° using a rotating-compensator ellipsometer⁷¹ (J.A. Woollam, M-2000XI).

The SE analyses of the α -FAPbI₃ layers are performed using a global error minimization scheme,⁷² in which the dielectric function is determined self-consistently using more than two samples with different layer thicknesses. For the α -FAPbI₃ analysis, two samples with thicknesses of 100 and 200 nm in Fig. 1(a) are used, and two sets of ellipsometry spectra are obtained from these samples [i.e., $(\psi, \Delta)_{100\text{nm}}$ and $(\psi, \Delta)_{200\text{nm}}$]. In our analysis, the dielectric function of the bulk layer $\epsilon_{\text{bulk}}(E)$ is extracted first from $(\psi, \Delta)_{100\text{nm}}$ using a mathematical inversion.⁷¹ For this analysis, an optical model consisting of a surface roughness layer/ α -FAPbI₃ bulk layer/SiO₂ (2 nm)/*c*-Si substrate is assumed. For the calculation of the surface-roughness optical properties, the Bruggeman effective-medium approximation (EMA)⁷¹ is employed. In our self-consistent SE

analysis, $\epsilon_{\text{bulk}}(E)$ obtained from $(\psi, \Delta)_{100\text{nm}}$ is applied further for the fitting analysis of $(\psi, \Delta)_{200\text{nm}}$. For this analysis, we employ an optical model with a void-rich interface layer on the substrate [i.e., surface roughness layer/ α -FAPbI₃ bulk layer/interface layer/SiO₂ (2 nm)/*c*-Si substrate], and the optical properties of the interface layer are also deduced from EMA assuming a mixture of α -FAPbI₃ and voids.

Figure 2 shows the SE fitting analysis of $(\psi, \Delta)_{200\text{nm}}$. In this figure, the open circles show experimental spectra of $(\psi, \Delta)_{200\text{nm}}$ and the solid lines indicate the fitting result calculated using $\epsilon_{\text{bulk}}(E)$ extracted from $(\psi, \Delta)_{100\text{nm}}$. As confirmed from Fig. 2, the calculated spectra show excellent fitting to the experimental spectra. In this analysis, however, the fitting quality degrades at $E \geq 3.0$ eV, most likely due to the effect of the rough surface. Thus, in the global-error-minimization analysis, the fitting is carried out in the region of $E \leq 3.0$ eV. In the subsequent analysis, we extract the final α -FAPbI₃ dielectric function from $(\psi, \Delta)_{100\text{nm}}$ by adjusting the bulk layer thickness slightly (within 2% of the total thickness) so that the ϵ_2 values become zero at $E < E_g$. However, the surface roughness thickness ($d_s = 1.7 \pm 0.1$ nm) obtained from the above analysis is smaller than the value of $d_{\text{rms}} = 10.9$ nm determined from AFM [Fig. 1(b)]. Thus, the amplitude of the α -FAPbI₃ dielectric function in the high energy region ($E > 3$ eV), which is excluded in the self-consistent SE analysis, could be underestimated by the effect of rough surface.⁵ A similar ellipsometry analysis is performed for δ -FAPbI₃ using the two samples in Fig. 1(a).

IV. DFT CALCULATION

The DFT calculations of various APbX₃ perovskite materials are implemented using a plane-wave ultrasoft pseudopotential method (Advance/PHASE software). For the calculations, the generalized gradient approximation within the Perdew-Burke-Ernzerhof scheme (PBE)⁷³ has been applied without considering spin-orbit coupling (SOC). Although the SOC effect is rather significant in hybrid perovskites,^{14-16,20,27,30,32} E_g of hybrid perovskites such as MAPbI₃ and FAPbI₃ can still be reproduced by the simple PBE calculation without incorporating SOC. This has been interpreted by the cancellation of errors induced by (i) the underestimation of E_g caused by the PBE functional and (ii) the overestimation of E_g generated without considering SOC.^{27,29,30} In more sophisticated calculations using the *GW* approximation^{14,15,20} and a hybrid functional,¹⁶ the experimental E_g values of MAPbI₃ and α -FAPbI₃ can be obtained by incorporating the SOC interaction. However, these high-level DFT

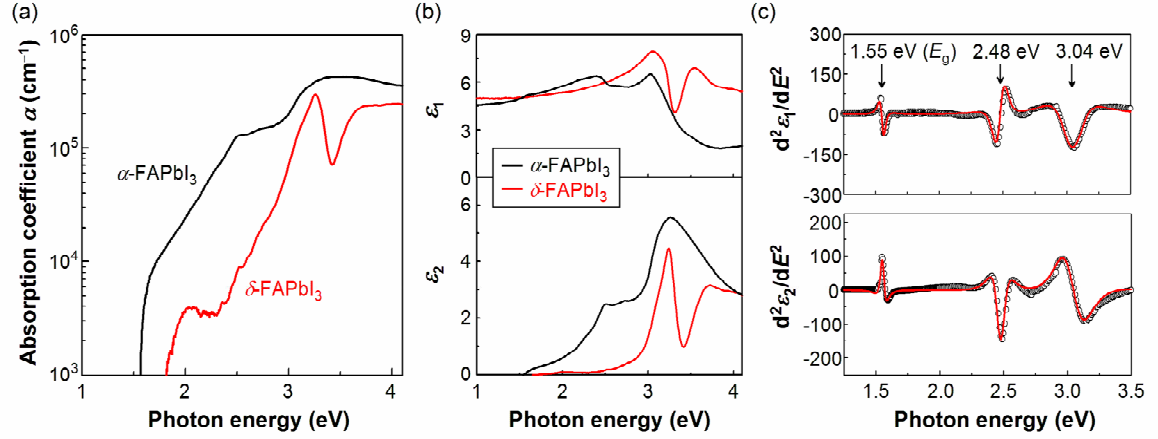


FIG. 3. (a) α spectra and (b) dielectric functions extracted from the α -FAPbI₃ layer (100 nm) and δ -FAPbI₃ layer (30 nm) in Fig. 1, together with (c) CP analysis of the α -FAPbI₃ dielectric function. In (c), the open circles denote the experimental data and the solid lines represent the theoretical fitting performed assuming three transitions in an energy region of $E \leq 3.5$ eV. The CP energies determined from the analysis are indicated by the arrows.

calculations lead to the band structures, which are essentially similar to that deduced from the PBE calculation.^{13,16,18} Thus, in this study, the simple PBE calculation is implemented without incorporating the SOC effect.

For α -FAPbI₃ and MAPbBr₃ crystals, we perform structural optimization within the cubic basis using a $6 \times 6 \times 6$ k mesh and a plane-wave cutoff energy of 500 eV until the atomic configuration converged to within 10 meV/Å. The dielectric functions are calculated based on a method developed by Kageshima et al.⁷⁴ For this calculation, we use a more dense $10 \times 10 \times 10$ k mesh to suppress distortion of calculated spectra.

V. RESULTS

A. Optical constants of hybrid perovskite materials

Figure 3 shows (a) the α spectra and (b) dielectric functions of the α -FAPbI₃ and δ -FAPbI₃ layers, together with (c) the critical point (CP) analysis of the α -FAPbI₃ dielectric function. These optical data are obtained from the self-consistent SE analyses described in Sec. III. The α spectrum of α -FAPbI₃ shows the sharp absorption onset

near E_g and the Urbach energy (E_U) determined assuming $\alpha \propto \exp(E/E_U)$ is 16 meV, supporting the suppressed tail state formation in α -FAPbI₃, as observed in MAPbI₃ ($E_U = 14\text{--}15$ meV)^{5,28} and (FA, Cs)Pb(I, Br)₃ ($E_U = 16$ meV).⁵⁶ It can be seen that the α value is significantly smaller in the δ phase, compared with the α phase, and the corresponding dielectric functions of these layers are quite different.

From the CP analysis shown in Fig. 3(c), we have further determined E_g of α -FAPbI₃. This analysis is carried out assuming three transitions in an energy region of $E \leq 3.5$ eV by using a procedure established previously.⁵ The open circles denote the experimental data and the solid lines represent the theoretical fitting. As a result, the CP energies of α -FAPbI₃ are determined to be 1.55 ± 0.01 eV, 2.48 ± 0.01 eV, and 3.04 ± 0.01 eV. The CP energy of 1.55 ± 0.01 eV corresponds to E_g (E_0 transition) and, in earlier studies, slightly smaller values in a range of 1.43–1.53 eV have been reported.^{3,45–48,53,59} The slight disagreement observed for E_g could be attributed to (i) the uncertainty in the E_g analysis and (ii) the underestimation of E_g due to extensive roughness of samples.⁵ The E_g value of MAPbI₃ determined from a similar CP analysis is 1.61 ± 0.01 eV.⁵ Thus, E_g changes only slightly in α -FAPbI₃, if compared with MAPbI₃.

Figure 4 compares (a) the α spectrum and (b) the dielectric function of α -FAPbI₃ obtained in this study with those of MAPbI₃ (Ref. 5), MAPbBr₃ (Ref. 27) and MAPbCl₃ (Ref. 27) reported earlier. The optical spectra of MAPbI₃ in Fig. 4 correspond to those obtained in our earlier study⁵ and have been extracted from a laser-evaporated MAPbI₃ layer using the self-consistent SE analysis, whereas the optical data of MAPbBr₃ and MAPbCl₃ have been obtained from the SE analyses of the single crystals.²⁷ We find that the α values of α -FAPbI₃ are notably smaller than those of MAPbI₃ and, at 1.7 eV, α of α -FAPbI₃ is half of that of MAPbI₃. Furthermore, although the overall ε_2 -spectral shapes of MAPbI₃ and α -FAPbI₃ are similar, the ε_2 amplitude of α -FAPbI₃ is roughly half of that of MAPbI₃ at $E < 3$ eV. Accordingly, the replacement of the center cation has a large impact on the absorption strength. The lower α observed in α -FAPbI₃ is consistent with the experimental fact that thicker absorber layers (~ 500 nm) are generally necessary for FAPbI₃-based perovskite solar cells,^{52,57–59} compared with MAPbI₃ solar cells (typically ~ 300 nm).¹ The ε_1 value at a low energy ($E = 1$ eV) also reduces from 5.26 (MAPbI₃) to 4.57 (α -FAPbI₃) and, therefore, the refractive index also varies by the effect of the center cation.

For the change of X in MAPbX₃, on the other hand, the whole dielectric function shifts systematically toward higher energy and the amplitude of the ε_2 spectrum gradually reduces in the lighter halogen atom [Fig. 4(b)]. In addition, a high-energy transition peak observed at 3.24 eV in MAPbI₃ splits into two peaks in MAPbBr₃ and

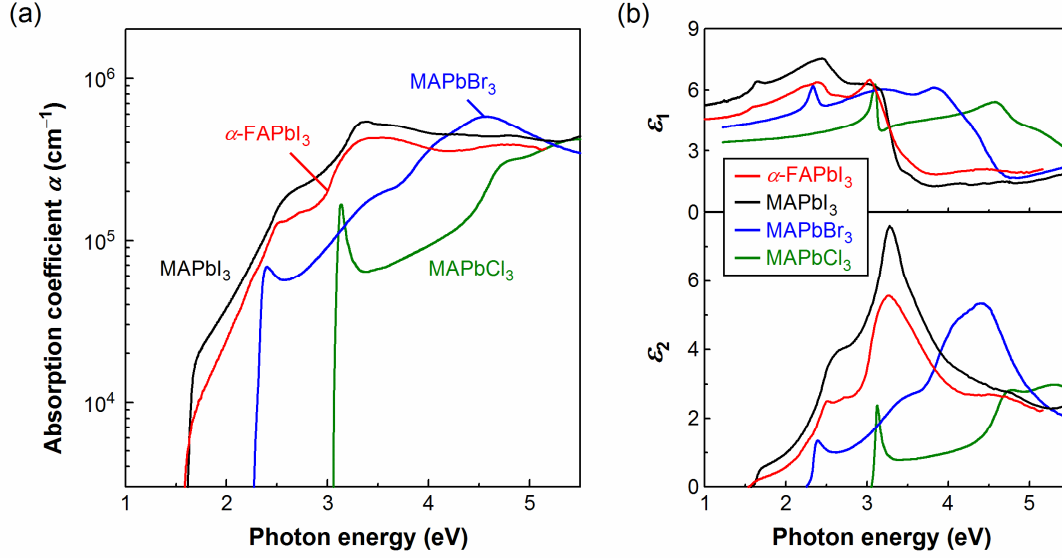


FIG. 4. (a) α spectra and (b) dielectric functions of α -FAPbI₃, MAPbI₃, MAPbBr₃ and MAPbCl₃. The optical data of α -FAPbI₃ in Fig. 3 and reported optical data of MAPbI₃ (Ref. 5), MAPbBr₃ (Ref. 27) and MAPbCl₃ (Ref. 27) are shown. The results of α -FAPbI₃ and MAPbI₃ are obtained from the polycrystalline materials, whereas those of MAPbBr₃ and MAPbCl₃ are extracted from the single crystals.

MAPbCl₃. The sharp absorption peaks observed near the E_g regions of MAPbBr₃ and MAPbCl₃ are caused by strong excitonic transitions⁷⁵ and the excitonic feature becomes stronger in the lighter halogen atom. The results of Fig. 4 show clearly that the A-site cation varies the oscillator strength of the optical transition, while the X-site halogen atom determines the transition energy.

The low α values observed in α -FAPbI₃ are justified further from external quantum efficiency (EQE) analysis. In particular, we analyze the EQE spectrum of a reported high-efficiency FAPbI₃ solar cell fabricated by a solution-based process⁵² using the α -FAPbI₃ dielectric function shown in Fig. 4(b). This FAPbI₃ solar cell has a structure of glass/SnO₂:F/compact TiO₂/mesoporous TiO₂ – α -FAPbI₃/ α -FAPbI₃/polytriarylamine (PTAA)/Au.⁵² For the optical constants of the component layers, we employ reported data,^{5,76} although the optical constants of spiro-OMeTAD [2,2',7,7'-tetrakis-(*N,N*-di-*p*-methoxyphenylamine) 9,9'-spirobifluorene]⁵ are used for the PTAA hole transport layer (HTL), as the optical constants of PTAA have not been reported and the absorption properties of PTAA⁷⁷ are similar to those of spiro-OMeTAD. The optical response within the mesoporous mixed-phase layer is expressed by two

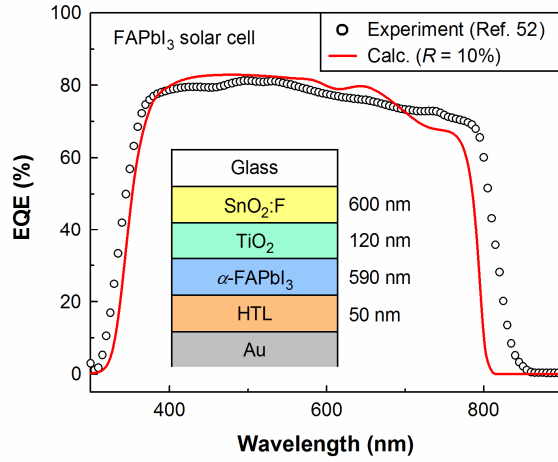


FIG. 5. EQE analysis of a FAPbI₃ hybrid perovskite solar cell using the α -FAPbI₃ optical constants shown in Fig. 4. The FAPbI₃ hybrid-perovskite solar cell fabricated by a solution process⁵² has a structure of glass/SnO₂:F/compact TiO₂/mesoporous TiO₂ – α -FAPbI₃/uniform α -FAPbI₃/polytriarylamine (PTAA)/Au. The open circles show the experimental data of Ref. 52, whereas the solid line represents the EQE spectrum calculated using an optical model consisting of glass/SnO₂:F (600 nm)/TiO₂ (120 nm)/ α -FAPbI₃ (590 nm)/HTL (50 nm)/Au. In the EQE calculation, R of the solar cell is assumed to be 10% in the whole wavelength region and the optical constants of spiro-OMeTAD are used for the HTL.

separate flat layers of TiO₂ and α -FAPbI₃ assuming a porosity of 60% for the TiO₂ layer.⁵ From these assumptions, we construct an optical model of glass/SnO₂:F (600 nm)/TiO₂ (120 nm)/ α -FAPbI₃ (590 nm)/spiro-OMeTAD (50 nm)/Au for the solar cell. The actual EQE calculation is implemented based on a reported procedure in which the absorptance of each component layer in solar cells is deduced from the optical admittance method using an experimental reflectance (R) spectrum.⁷⁸ However, since the R spectrum of the perovskite solar cell has not been reported, we perform the EQE calculation assuming a fixed R value of 10%, as observed in MAPbI₃ solar cells having similar structures ($R = 2\text{--}10\%$).² The EQE spectrum of the solar cell is then determined assuming 100% collection of photocarriers generated within the α -FAPbI₃ absorber layer.

Figure 5 shows the experimental EQE spectrum of the FAPbI₃ hybrid perovskite solar cell⁵² (open circles) and the simulated EQE spectrum obtained from the above calculation procedure assuming $R = 10\%$ (solid line). As confirmed from Fig. 5, the

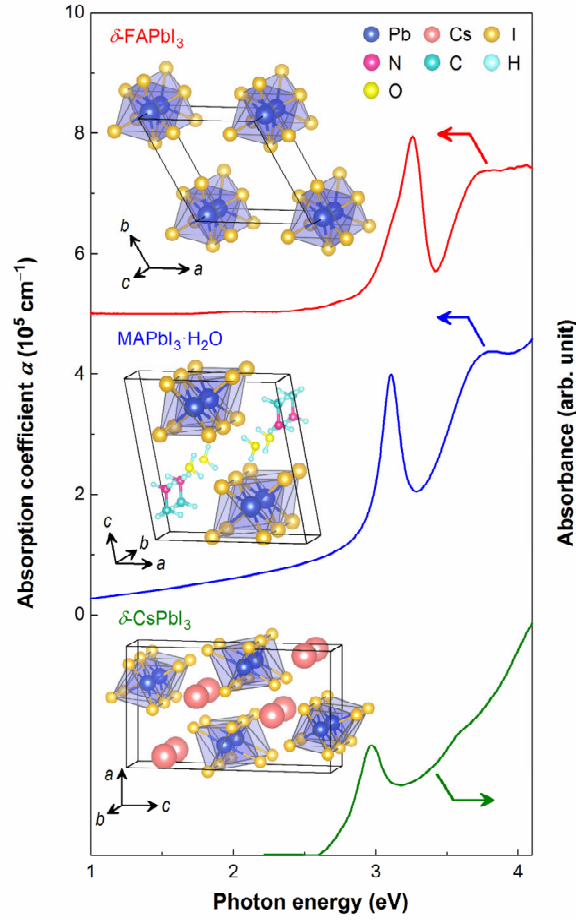


FIG. 6. Absorption spectra of δ -FAPbI₃, MAPbI₃·H₂O and δ -CsPbI₃. The α spectrum of δ -FAPbI₃ corresponds to that shown in Fig. 3(a), whereas the absorption spectra of MAPbI₃·H₂O and δ -CsPbI₃ are taken from Ref. 43 and Ref. 79, respectively. The α spectrum of δ -FAPbI₃ is shifted by $5 \times 10^5 \text{ cm}^{-1}$ for clarity. The insets show the crystal structures reported for δ -FAPbI₃ (Ref. 3), MAPbI₃·H₂O (Ref. 80) and δ -CsPbI₃ (Ref. 3). In the structure of δ -FAPbI₃, the FA cations are not shown due to the uncertainty of the exact configuration.

overall EQE response in the solar cell is reproduced quite well in our simulation. However, the absorption onset of α -FAPbI₃ observed in the experimental EQE spectrum is $\sim 840 \text{ nm}$ and shows a slight red shift, compared with the EQE calculation result ($\sim 800 \text{ nm}$). This could be attributed to (i) the light scattering in the solar cell, which is not modeled in our EQE analysis or (ii) the tail-state absorption in the solar cell.

In Fig. 6, on the other hand, the α spectrum of δ -FAPbI₃ is compared with the

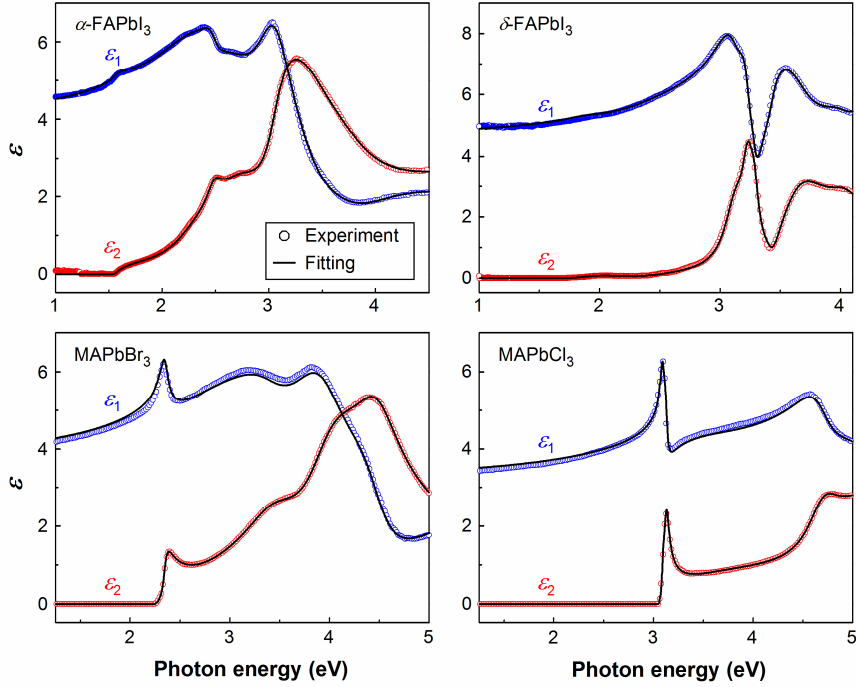


FIG. 7. Parameterization of the dielectric functions of α -FAPbI₃, δ -FAPbI₃, MAPbBr₃ and MAPbCl₃ using Tauc-Lorentz transition peaks. The open circles show the experimental dielectric functions of α -FAPbI₃ and δ -FAPbI₃ shown in Fig. 3(b) and MAPbBr₃ (Ref. 27) and MAPbCl₃ (Ref. 27) shown in Fig. 4(b), while the solid lines indicate the fitting results. The model parameters are summarized in Table I.

absorption spectra of MAPbI₃·H₂O (Ref. 43) and orthorhombic CsPbI₃ (δ -CsPbI₃),⁷⁹ which also have one-dimensional crystal structures. It can be seen that all the PbI₆-based compounds in Fig. 6 exhibit similar absorption peaks at $E = 3.0$ - 3.3 eV with weak shoulder peaks at 3.6 - 3.8 eV. The sharp peak at 3.1 eV in MAPbI₃·H₂O cannot be reproduced in the DFT calculation within the PBE¹¹ and has been attributed to the excitonic transition.⁴³ As confirmed from the insets of Fig. 6, the crystal structure of δ -FAPbI₃ (Ref. 3) is slightly different from those of MAPbI₃·H₂O (Ref. 80) and δ -CsPbI₃ (Ref. 3), although the absorption feature of δ -FAPbI₃ is quite similar to those of MAPbI₃·H₂O and δ -CsPbI₃.

The dielectric functions of α -FAPbI₃, MAPbBr₃ and MAPbCl₃ in Fig. 4(b) can be parameterized by assuming several Tauc-Lorentz (TL) transitions.⁸¹ In the TL model, a dielectric function peak is modeled by a total of five parameters: the amplitude parameter (A), broadening parameters (C), peak transition energy (E_p), Tauc optical gap

TABLE I. Tauc-Lorentz parameters extracted from the dielectric function modeling shown in Fig. 7.

Material	Peak	E_p (eV)	A (eV)	C (eV)	E_T (eV)	$\epsilon_1(\infty)$
α -FAPbI ₃	1	1.557	10.018	0.099	1.543	1.462
	2	1.566	8.849	0.498	1.521	0
	3	2.344	9.041	0.794	1.618	0
	4	2.486	1.028	0.171	1.740	0
	5	2.712	20.435	0.755	2.093	0
	6	3.083	66.516	0.417	2.726	0
	7	3.190	98.353	0.657	2.918	0
	8	3.897	131.316	3.018	3.882	0
δ -FAPbI ₃	1	1.893	1.573	0.404	1.667	2.455
	2	2.291	15.657	1.898	2.288	0
	3	3.127	2.182	0.232	1.690	0
	4	3.232	1.563	0.118	1.803	0
	5	3.285	0.411	0.078	1.695	0
	6	3.439	367.887	0.233	3.411	0
	7	3.611	72.513	0.366	3.398	0
	8	4.021	3.777	0.291	3.305	0
	9	4.638	776.547	0.202	4.388	0
MAPbBr ₃	1	2.258	14.194	0.022	2.245	0.011
	2	2.298	50.951	0.110	2.257	0
	3	2.343	140.251	0.090	2.305	0
	4	2.425	48.060	2.641	2.382	0
	5	3.416	14.262	1.002	2.412	0
	6	3.949	78.865	0.663	3.489	0
	7	4.466	6.204	0.620	2.428	0
	8	8.469	41.650	0.070	2.905	0

TABLE I. (Continued.)

Material	Peak	E_p (eV)	A (eV)	C (eV)	E_g (eV)	$\varepsilon_1(\infty)$
MAPbCl ₃	1	3.065	24.330	0.012	3.045	0.076
	2	3.096	177.556	0.046	3.043	0
	3	3.125	219.273	0.052	3.071	0
	4	3.199	34.078	1.516	3.099	0
	5	4.695	10.013	0.397	3.733	0
	6	5.279	17.475	1.421	3.051	0
	7	9.718	209.001	0.053	6.544	0

(E_T) and the ε_1 contribution at high energy [$\varepsilon_1(\infty)$]. Figure 7 summarizes the results of dielectric function modeling performed for FAPbI₃, MAPbBr₃ and MAPbCl₃ using the TL peaks. In this figure, the open circles denote the optical data shown in Fig. 4, whereas the solid lines indicate the calculation results. The TL parameters for FAPbI₃, MAPbBr₃ and MAPbCl₃ are summarized in Table 1. From these model parameters, the α spectra of these materials, shown in Fig. 4(a), can be expressed. Similar parameterization has already been performed for MAPbI₃ in our earlier study.⁵

B. Optical transitions in α -FAPbI₃ and MAPbBr₃

To understand the optical transitions in α -FAPbI₃ and MAPbBr₃ crystals, the DFT calculations are implemented assuming pseudocubic structures. Figure 8(a) shows the α -FAPbI₃ and MAPbBr₃ crystal structures determined from the DFT. In Fig. 8(a), a , b , and c indicate the axes of the unit cell. From the structural optimization, we obtain lattice parameters of $a = 6.416$ Å, $b = 6.236$ Å, and $c = 6.353$ Å with $\alpha = \beta = \gamma = 90.00^\circ$ (α -FAPbI₃) and $a = 5.934$ Å, $b = 5.919$ Å, and $c = 5.936$ Å with $\alpha = \gamma = 90.00^\circ$ and $\beta = 89.94^\circ$ (MAPbBr₃). In the DFT result for α -FAPbI₃, the lattice parameter of a is expanded slightly, compared with b and c , due to the steric effect of FA⁺, while the lattice parameters are almost the same in MAPbBr₃. The average lattice parameters obtained from the calculations (6.335 Å in α -FAPbI₃ and 5.930 Å in MAPbBr₃) show excellent agreement with the experimental results reported for α -FAPbI₃ (6.362 Å in Ref. 50) and MAPbBr₃ (5.94 Å in Ref. 10). In α -FAPbI₃, the introduction of the large center cation leads to the formation of collinear I-Pb-I bonds, which are more closer to 180°, if compared with MAPbI₃.⁵

In many earlier studies, α -FAPbI₃ is reported to have a trigonal symmetry.^{3,45,47-49} Nevertheless, a recent neutron-powder diffraction study⁵⁰ confirms that α -FAPbI₃ has a

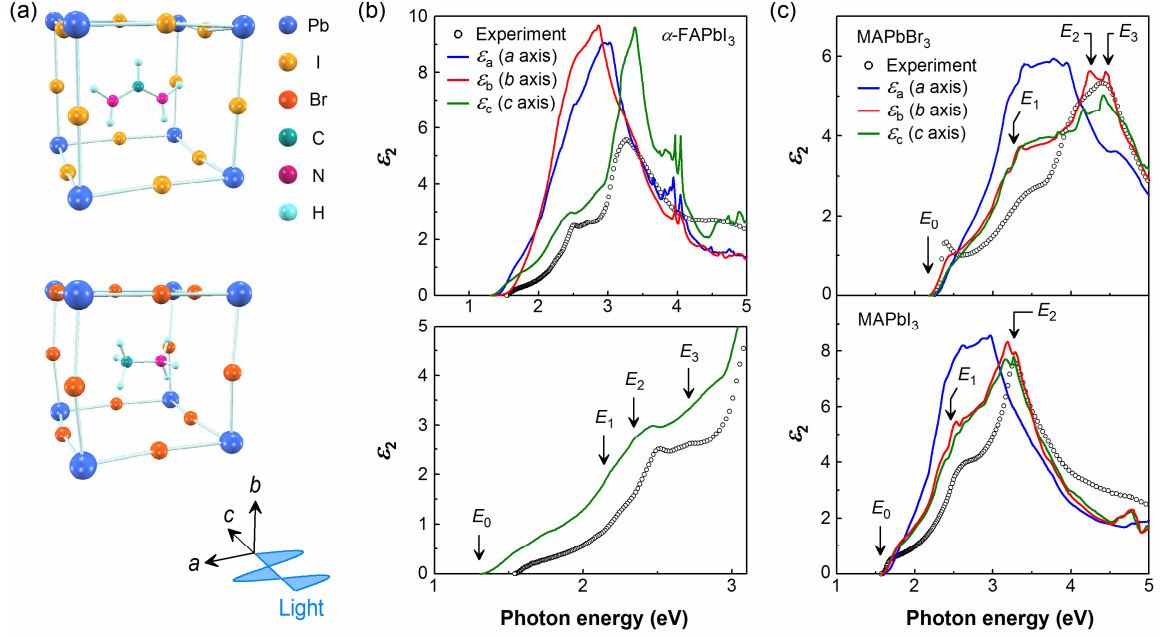


FIG. 8. (a) Pseudocubic crystal structures of α -FAPbI₃ and MAPbBr₃ obtained from the DFT calculations, and ϵ_2 spectra of (b) α -FAPbI₃ and (c) MAPbBr₃ and MAPbI₃, obtained from the experiments (open circles) and DFT calculations (solid lines). In (b) and (c), the experimental results correspond to those shown in Fig. 4(b) (MAPbBr₃: Ref. 27, MAPbI₃: Ref. 5), and ϵ_a , ϵ_b and ϵ_c represent the ϵ_2 spectra calculated assuming the light polarization along the a , b , and c axes shown in (a), respectively. The arrows indicate the transition energies determined by the DFT analyses. In (b), the ϵ_2 spectra in two different energy regions are shown for clarity. In (c), the DFT calculation result for MAPbBr₃ has been shifted toward higher energy by 0.22 eV to obtain better matching with the experimental spectrum, whereas the results of MAPbI₃ are adopted from our earlier study⁵.

simpler cubic symmetry with the N-C-N plane parallel to the a - b plane (or the line connecting two N atoms of FA⁺ is parallel to the a axis). This experimental result is consistent with our DFT result shown in Fig. 8(a). The configuration of MA⁺ in MAPbBr₃ is essentially similar to that in MAPbI₃ (Ref. 5) and the C-N bond of MA⁺ is almost parallel to the a axis.

In Fig. 8(b), the experimental ϵ_2 spectrum of α -FAPbI₃ is compared with the ϵ_2 spectra that are calculated for the different polarization states with directions parallel to

the a , b , and c axes in Fig. 8(a). The DFT calculation reveals the highly anisotropic optical behavior of α -FAPbI₃ and the ϵ_2 spectra for the a and b axes (ϵ_a and ϵ_b) exhibit quite different shapes from that for the c axis (ϵ_c). In Fig. 8(b), the ϵ_2 spectra in two different energy regions are shown for ϵ_c . Quite remarkably, ϵ_c reproduces all the fine absorption features observed experimentally at $E < 3$ eV and shows the excellent overall agreement with the experimental result. At higher energies ($E > 3$ eV), however, the amplitude of the experimental ϵ_2 spectrum is much lower than that of the calculation (ϵ_c). The disagreement in the high energy region may originate from SE analysis errors induced by the rough surface structures of the α -FAPbI₃ samples, as mentioned in Sec. III. In Fig. 8(b), the arrows represent the optical transitions in the Brillouin zone, determined from the polarization-dependent DFT analysis described below.

In Fig. 8(c), the ϵ_2 spectra of MAPbBr₃ calculated from the structure of Fig. 8(a) are compared with the experimental ϵ_2 spectrum of Ref. 27. The experimental and DFT data of MAPbI₃ in Fig. 8(c) are taken from our previous study,⁵ in which the DFT calculation was performed in a similar way. For MAPbBr₃, all the calculated spectra have been shifted toward higher energy by 0.22 eV to match the DFT result with the experimental result. As confirmed from Fig. 8(c), MAPbBr₃ and MAPbI₃ show the strong anisotropic behavior, and the experimental ϵ_2 spectra of MAPbBr₃ and MAPbI₃ are reproduced surprisingly well in the calculated ϵ_2 spectra of ϵ_b and ϵ_c . The ϵ_a spectrum of MAPbBr₃ is similar to that reported in a previous DFT study.⁶³ The arrows for MAPbBr₃ in Fig. 8(c) show the result of our optical transition analysis described below. In our study, the E_0 (E_g), E_1 and E_2 transitions in MAPbI₃ are attributed to the non-excitonic direct transitions at the R , M and X points in the pseudocubic Brillouin zone.⁵ For the assignment of the interband transitions in MAPbI₃, a similar result has also been reported.²⁷

The DFT calculations in this study are performed without incorporating electron-hole interactions (or exciton formation). Thus, the band-edge excitonic transition observed in MAPbBr₃ at 2.4 eV cannot be reproduced in our DFT calculation and, consequently, the calculated ϵ_2 becomes lower than the experimental ϵ_2 near the E_g region. For α -FAPbI₃, the calculated ϵ_2 values are larger than the experimental ϵ_2 values, indicating the negligible contribution of excitons in the light absorption process. Non-excitonic nature of MAPbI₃ has already been confirmed earlier.^{5,19,23}

We further calculate the band structure and density of states (DOS) of α -FAPbI₃ [Fig. 9(a)] and MAPbBr₃ [Fig. 9(b)]. For MAPbBr₃, however, the energy positions of all the conduction bands are shifted upward by 0.22 eV (scissors operation).⁸² The high symmetry points in the Brillouin zone defined by the reciprocal lattices ($a^* = 2\pi/a$, $b^* =$

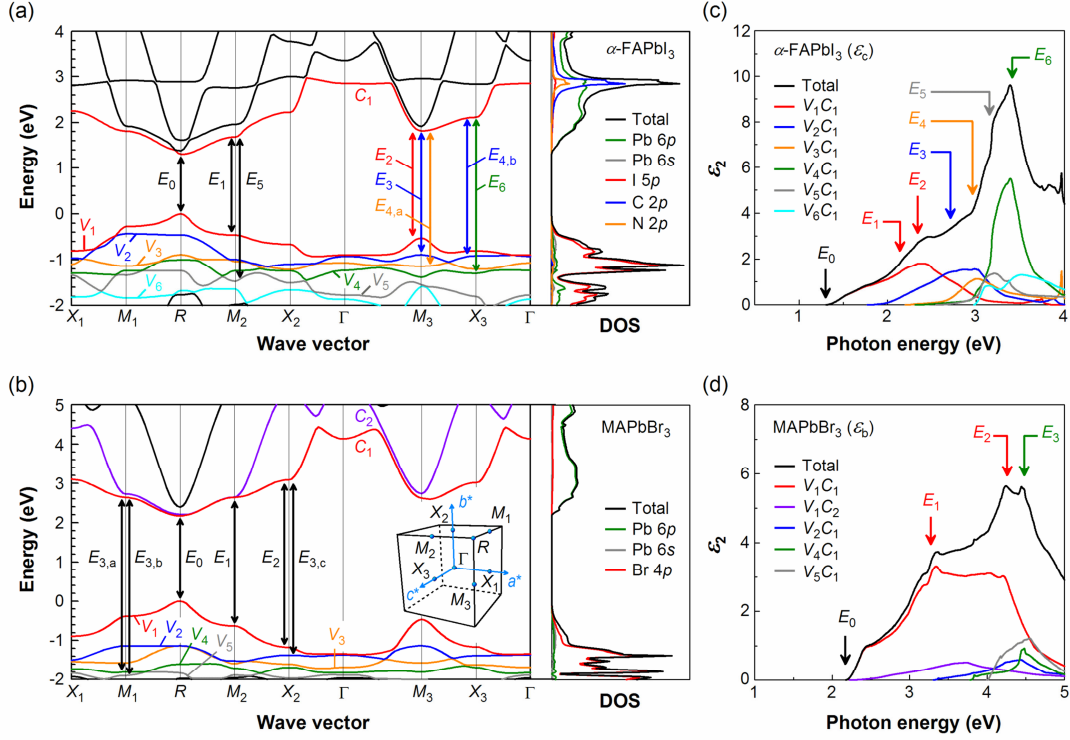


FIG. 9. Band structure and DOS of (a) α -FAPbI₃ and (b) MAPbBr₃ pseudocubic crystals, together with the contributions of various interband transitions to (c) the ϵ_c spectrum of α -FAPbI₃ and (d) the ϵ_b spectrum of MAPbBr₃. In (a) and (b), V_j and C_j denote the j th valence and conduction bands from VBM and CBM, respectively. The optical transitions determined by the polarization-dependent DFT analyses are indicated by arrows, and the partial DOS distributions are also indicated. In (a), the transition energies of $E_{4,a}$ at the M_3 point and $E_{4,b}$ at the X_3 point are almost identical. In (b), all the conduction bands have been shifted upward by 0.22 eV to improve the agreement with the experimental result. The inset shows the high symmetry points in the Brillouin zone defined by the reciprocal lattices ($a^* = 2\pi/a$, $b^* = 2\pi/b$, $c^* = 2\pi/c$) of the assumed pseudocubic structure. The transition energies of $E_{3,a}$ (M_1 point), $E_{3,b}$ (M_1 point) and $E_{3,c}$ (X_2 point) are almost identical. In (c) and (d), the ϵ_2 spectra denoted as “Total” correspond to ϵ_c of α -FAPbI₃ and ϵ_b of MAPbBr₃ in Fig. 8, and V_jC_k denotes the interband transition from the j th valence band to the k th conduction band. The transition energies (E_{0-6}) determined from the DFT analysis are also indicated. In (c), only the transitions with a peak amplitude of $\epsilon_2 > 1.0$ are shown for clarity. In (d), only the transitions with a peak amplitude of $\epsilon_2 > 0.5$ are shown for clarity.

$2\pi/b$, $c^* = 2\pi/c$) are shown in the inset of Fig. 9(b). Since the assumed pseudocubic structures are distorted, the energy positions of M_{1-3} and X_{1-3} in the Brillouin zone differ slightly. In Figs. 9(a) and 9(b), V_j and C_j denote the j th valence and conduction bands from the valence band maximum (VBM) and the conduction band minimum (CBM), respectively. The V_1 mainly consists of the I $5p$ state in α -FAPbI₃ and the Br $4p$ state in MAPbBr₃, whereas C_1 is dominated by the Pb $6p$ in both α -FAPbI₃ and MAPbBr₃. It can be seen that the shapes of C_1 and V_j ($j \leq 4$) in α -FAPbI₃ and MAPbBr₃ are quite similar, although the energy positions of these bands are different. In the case of α -FAPbI₃, there is an additional conduction band at the energy position of ~ 2.9 eV in Fig. 9(a). This band is due to the π -state of the sp^2 C atom in FA⁺ and the DOS in this energy region increases sharply by the presence of the C $2p$ π -state.

To determine the optical transitions in α -FAPbI₃ and MAPbBr₃, the contribution of each interband transition to the ε_2 spectrum is calculated for ε_c of α -FAPbI₃ and ε_b of MAPbBr₃, and the results are shown in Figs. 9(c) and 9(d). In these figures, the ε_2 spectra denoted as “Total” correspond to those in Fig. 8, and $V_j C_k$ denotes the ε_2 contribution induced by the transition from the j th valence band to the k th conduction band. In Figs. 9(c) and 9(d), only the transitions with amplitudes of $\varepsilon_2 > 1.0$ (α -FAPbI₃) and $\varepsilon_2 > 0.5$ (MAPbBr₃) are shown for clarity. Based on the band structure and the ε_2 contributions of $V_j C_k$, we select the optical transitions at high symmetry points that satisfy van Hove singularities⁷⁰ in k space: i.e., $\nabla_{\mathbf{k}} [E_c(\mathbf{k}) - E_v(\mathbf{k})] = 0$, where $E_c(\mathbf{k})$ and $E_v(\mathbf{k})$ show the energies of the conduction and valence bands, respectively. The optical transitions determined from the DFT analyses are denoted by the arrows in Fig. 9. In Fig. 8, the transition energies of E_{0-3} determined by the above procedure have been shown.

As confirmed from Figs. 9(a) and 9(b), α -FAPbI₃ and MAPbBr₃ are direct transition semiconductors with the E_0 (E_g) transitions at the R point (cubic symmetry).^{27,63-65} Our analyses further show that the interband transitions in α -FAPbI₃ are dominated by the transitions to C_1 , and C_j ($j \geq 2$) do not involve in the visible-light absorption. As a result, in α -FAPbI₃, the interband transitions at low energies ($E < 3.2$ eV) are characterized by V_j ($j \leq 5$) \rightarrow C_1 transitions that occur predominantly at the M point (E_{1-5} transitions), whereas the intense ε_2 peak at 3.4 eV is attributed to the $V_4 C_1$ transition at the X_3 point (E_6 transition). It should be noted that the E_1 and E_2 peaks of α -FAPbI₃ originate from the same interband transition of $V_1 C_1$ at the M point. However, the energy positions of $V_1 C_1$ at the M_2 point (E_1 transition) and M_3 point (E_2 transition) are different. This can be interpreted by the large difference in the lattice parameters ($a = 6.416$ Å and $b = 6.236$ Å) and the resulting reciprocal lattices [$a^* \rightarrow M_3$ and $b^* \rightarrow M_2$ in the Brillouin

zone of Fig. 9(b)]. Accordingly, the E_1 and E_2 peaks observed in the experimental spectrum [Fig. 8(b)] support the rather significant distortion of α -FAPbI₃ crystals.

In MAPbBr₃, on the other hand, the optical transition in the visible region occurs predominantly by the V_1C_1 transition [Fig. 9(d)], while the V_1C_2 transition shows a weak contribution. The overall optical transitions in MAPbBr₃ are quite similar to those of MAPbI₃ (Ref. 5) and the E_1 , E_2 and E_3 peaks that appear in ϵ_b of MAPbBr₃ are attributed primarily to the transitions at the M_2 (V_1C_1), X_2 (V_1C_1) and M_1 (V_4C_1 and V_3C_1) points, respectively. In contrast to MAPbBr₃, MAPbI₃ shows a single transition peak in the high energy region [E_2 transition in Fig. 8(c)], as the transition energies at the X_2 (V_1C_1) and M_1 (V_4C_1) points are almost the same in MAPbI₃.⁵ For MAPbBr₃, the optical transition analysis has been made by the self-consistent GW ²⁷ and the PBE,⁶³ but the proposed assignments of the transition peaks are slightly different from our result shown in Fig. 9(b). The DFT results in Fig. 9 indicate clearly that the interband transitions in the visible region occur predominantly from the valence state of the X atom to the Pb-derived conduction state (i.e., $V_j \rightarrow C_1$).

The E_g of α -FAPbI₃ obtained from the DFT calculation [1.30 eV in Fig. 9(a)] is slightly smaller than that of MAPbI₃ (1.56 eV).⁵ It has been confirmed previously that E_g of APbI₃ is determined primarily by the I–Pb–I bond angle of the PbI₃[−] cage.^{17,20,44} More specifically, when the cation size is larger, the I–Pb–I bond angle becomes collinear ($\sim 180^\circ$), and resulting E_g reduces slightly.^{17,20,44} The decrease in E_g at a larger I–Pb–I angle has been explained by the anti-bonding character of the Pb–I bond.^{17,44} Consequently, E_g of APbI₃ increases with the order of FA⁺ < MA⁺ < Cs⁺.¹⁷ As mentioned earlier, however, the experimental E_g values of α -FAPbI₃ (1.55 eV) and MAPbI₃ (1.61 eV) are rather similar.

Figure 10 shows the α spectra of FAPbI₃ calculated by the PBE without SOC (this study) and the GW approximation with SOC,²⁰ together with the experimental spectrum of Fig. 4(a). The α spectrum of the PBE without SOC, calculated from ϵ_c of Fig. 8(b), shows similar trend with the experimental result. Although the anisotropic optical properties of FAPbI₃ have not been reported in earlier DFT studies,^{20,65} the α spectrum derived from the simple PBE shows quite good agreement with that calculated from the GW method with SOC. In particular, the peak energies calculated by these DFT methods are quite consistent. However, the α spectra obtained from these calculations show different shapes near the E_g region. As known well,^{14,15,20,30} when the DFT calculations are implemented by incorporating SOC, all the bands split into two bands. This effect is particularly strong in the conduction bands³⁰ as the conduction bands are derived predominantly from the heavy Pb atom that exhibits a large SOC effect.

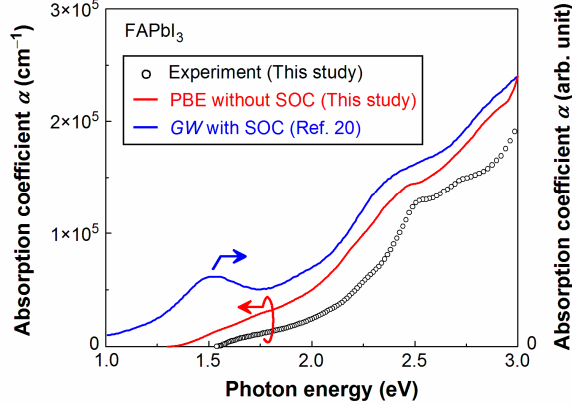


FIG. 10. α spectra of FAPbI₃ obtained from the experiment (open circles) and the DFT calculations based on the PBE without SOC (this study) and the GW method with SOC²⁰ (solid lines). The α spectrum of the PBE without SOC is obtained from ϵ_c shown in Fig. 8(b).

Accordingly, the α peak observed at 1.5 eV in the GW -SOC result could be attributed to the effect of the conduction band splitting by SOC. It has been confirmed that the SOC-induced band splitting near the fundamental gap varies rather significantly with the orientation of the A-site cation^{31,32,64} and the absorption characteristics near E_g may be influenced strongly by the position and orientation of the A-site cation.

C. Effects of A and X on the light absorption

The quite strong anisotropy observed in the DFT-derived dielectric functions in Fig. 8 can be understood by considering the strong interaction between the A-site cation and the surrounding X-site halogen atoms. Figure 11 shows the charge density profiles of (a) α -FAPbI₃ and (b) MAPbI₃ in the energy region of $-0.6 \sim -0.4$ eV from VBM ($E = 0$ eV). In Fig. 11, the charge density decreases with the order of red > yellow > green > blue with red being the highest. The charge density profiles in Fig. 11 represent the valence charge densities for the E_2 transition in α -FAPbI₃ and the E_1 transition in MAPbI₃ at the M point (V_1C_1). More specifically, in the case of α -FAPbI₃, the energy position of V_1 at the M_3 point is -0.52 eV from VBM [Fig. 9(a)] and thus the valence charge density in this energy regime is responsible for the E_2 transition that occurs at 2.34 eV [see Fig. 9(c)]. For the E_1 transition of MAPbI₃ at 2.46 eV, the position of V_1 at the M_2 point is located at a similar energy of -0.44 eV from VBM.⁵ Here, we particularly consider the

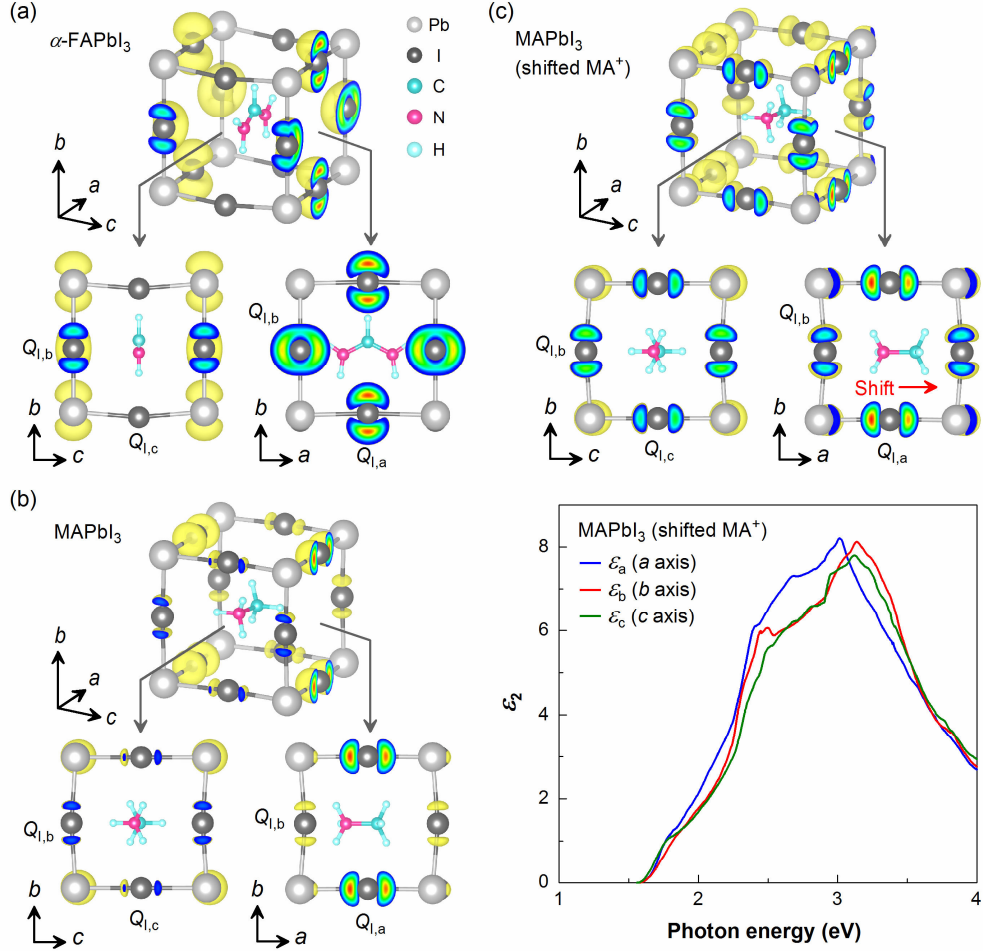


FIG. 11. Charge density profiles of (a) α -FAPbI₃, (b) MAPbI₃ and (c) hypothetical MAPbI₃ with shifted MA⁺ in the energy region of $-0.6 \sim -0.4$ eV from VBM ($E = 0$ eV). These profiles represent the valence charge densities for the E_2 transition (α -FAPbI₃) and the E_1 transition (MAPbI₃) at the M point (V_1C_1). The charge density decreases with the order of red > yellow > green > blue with red being the highest. The valence charges of the I atoms along the a , b , and c axes are indicated as $Q_{I,a}$, $Q_{I,b}$ and $Q_{I,c}$, respectively. In (c), the N atom of MA⁺ is shifted to the center position of the C–N bond in (b) and the ϵ_2 spectra obtained from this hypothetical MAPbI₃ structure are also shown.

charge density distribution at the M point, as the visible light absorption in the hybrid perovskites is determined essentially by the interband transitions near the M point (V_1C_1). The result of MAPbI₃ in Fig. 11(b) is obtained from the optimized MAPbI₃ structure reported in our previous study.⁵

In Figs. 11(a) and 11(b), the charge density profiles in the same energy region ($-0.6 \sim$

–0.4 eV) are shown, but the distributions of the I-5*p* charge density in α -FAPbI₃ and MAPbI₃ are significantly different. Specifically, the I-5*p* valence electron of α -FAPbI₃ concentrates on the I atoms along the *a* and *b* axes, and the valence charges of these I atoms ($Q_{I,a}$ and $Q_{I,b}$, respectively) are far larger than that of the *c* axis direction ($Q_{I,c}$). In contrast, the valence charge distribution is more uniform in MAPbI₃, although $Q_{I,a}$ is larger than $Q_{I,b}$ and $Q_{I,c}$.

We find that the distribution of $Q_{I,a-c}$ is determined by the strong interaction between the N and I atoms. It is now established that, in MAPbI₃ (Refs. 20, 32, 35-39) and FAPbI₃ (Refs. 20, 50), hydrogen bonding is formed between the I and H–N, which can be expressed as I(δ^-)···H(δ^+)–N(δ^-). Here, δ^+ and δ^- represent the positive and negative partial charges, respectively. The absolute value of δ is governed predominantly by the electronegativity, and the hydrogen bonding of I···H–N leads to the reduction of the N–I distance, as confirmed from Fig. 11(b). Our systematic DFT calculations reveal that the distribution of $Q_{I,a-c}$ is controlled primarily by the N–I distance and $Q_{I,a-c}$ reduces significantly when the N–I distance is smaller (anti-coupling effect). In α -FAPbI₃, for example, $Q_{I,c}$ becomes quite small due to the intense anti-coupling effect induced by the shorter N–I distance, and the valence charge concentrates on the *a*-*b* plane. In MAPbI₃, larger $Q_{I,a}$, compared with $Q_{I,b}$ and $Q_{I,c}$, can also be interpreted by the strong anti-coupling interaction as the N atom locates close to the *b*-*c* plane due to the effect of hydrogen bonding.

The highly anisotropic optical transitions at the *M* point can be explained almost completely by the anti-coupling effect. For the E_2 transition of α -FAPbI₃ at 2.34 eV, for example, ε_b shows the highest ε_2 value, while ε_c indicates the lowest value [Fig. 8(b)]. As confirmed from Fig. 11(a), $Q_{I,a}$ shows the highest value among $Q_{I,a-c}$ and the charge density distribution of $Q_{I,a}$ is oriented along the *b* axis, which in turn increases the polarizability in this direction significantly. Consequently, ε_b of α -FAPbI₃ exhibits the maximum ε_2 value, while very low $Q_{I,c}$ leads to the drastic reduction of the transition probability and results in quite small ε_c . In the case of MAPbI₃, the charge density profile of $Q_{I,a}$ is aligned along the *a* axis [Fig. 11(b)], therefore increasing the ε_a value at 2.46 eV (E_1 transition), whereas we observe $\varepsilon_b \sim \varepsilon_c$ since $Q_{I,b} \sim Q_{I,c}$, as confirmed from Fig. 8(c).

To justify quite strong anti-coupling effect in the hybrid perovskites, the charge density profile of MAPbI₃ is calculated by changing the position of MA⁺ [Fig. 11(c)]. For this calculation, the N atom position of MA⁺ is shifted intentionally and is placed at the center position of the C–N bond in Fig. 11(b). In this hypothetical configuration, the charge density distribution of –0.6 ~ –0.4 eV becomes more uniform, compared with

the case of Fig. 11(b), as $Q_{1,b}$ and $Q_{1,c}$ increase due to the increased N-I distance. More importantly, as the result of the charge redistribution, the strong anisotropic behavior disappears in the calculated dielectric functions [Fig. 11(c)]. This effect can be seen clearly by comparing the polarization-dependent ϵ_2 spectra of MAPbI₃ in Fig. 8(c) with those in Fig. 11(c).

One very important result in Fig. 8 is that, among the ϵ_2 spectra calculated for different light polarizations, the ϵ_2 spectrum having the lowest ϵ_2 values in the visible region shows the best match with the experimental data. This result indicates that the visible-light absorption in the actual hybrid perovskites is modified significantly by the anti-coupling effect. In other words, although the Pb-derived conduction band (C_1) is independent of A, the electronic states of the I and Br are influenced strongly by the hydrogen bonding of the A-site cation.

To clarify the anti-coupling interaction further, we calculate the dielectric functions of various APbX₃ perovskites with different A-site cations (FA⁺, MA⁺, NH₄⁺, Cs⁺) and X-site halogen atoms (I, Br, Cl). In particular, the APbX₃ dielectric functions are obtained by replacing the A-site cation in identical PbI₃⁻, PbBr₃⁻ and PbCl₃⁻ structures to determine the effect of the A-site cation on the optical absorption. For the PbX₃⁻ structures, we employ the configurations that are determined from the structural optimization of MAPbX₃. In our calculations, the position and orientation of the A-site cation within a fixed PbX₃⁻ cage are optimized and, in the resulting CsPbX₃ structures, Cs⁺ locates near the center position of the unit cell. In the calculation of α -FAPbX₃, however, the FA⁺ orientation in Fig. 8(a) is assumed because a quite different FA⁺ orientation is obtained when FA⁺ is relaxed within the PbX₃⁻ derived from MAPbX₃.

Figure 12 shows the ϵ_2 spectra of (a) α -FAPbX₃, (b) MAPbX₃ and (c) CsPbX₃ calculated from the above procedure, together with corresponding ϵ_2 spectra of (d) α -FAPbX₃, (e) MAPbX₃ and (f) CsPbX₃ obtained by applying the sum rule, which is explained below. In Fig. 12, only the ϵ_2 spectra of ϵ_c (α -FAPbX₃) and ϵ_b (MAPbX₃ and CsPbX₃) are shown and the bars indicate the energy positions of the E_1 transition at the M_2 point (V_1C_1). The calculated dielectric functions of NH₄PbX₃ are almost the same with those of MAPbX₃ shown in Fig. 12(b). As confirmed from Figs. 12(a)-(c), the overall ϵ_2 -spectral shapes are similar when the ϵ_2 spectra of the same X are compared. However, the ϵ_2 amplitude varies rather significantly with the A-site cation and the ϵ_2 value for the E_1 transition, indicated by the bar in Fig. 12, increases from $\epsilon_2 = 3.1$ (α -FAPbI₃) to 4.9 (CsPbI₃). Although the dielectric functions of CsPbX₃ have not been reported, the shape of the absorbance spectrum reported for CsPbI₃ (Refs. 83, 84) is quite similar to that shown in Fig. 12(c).

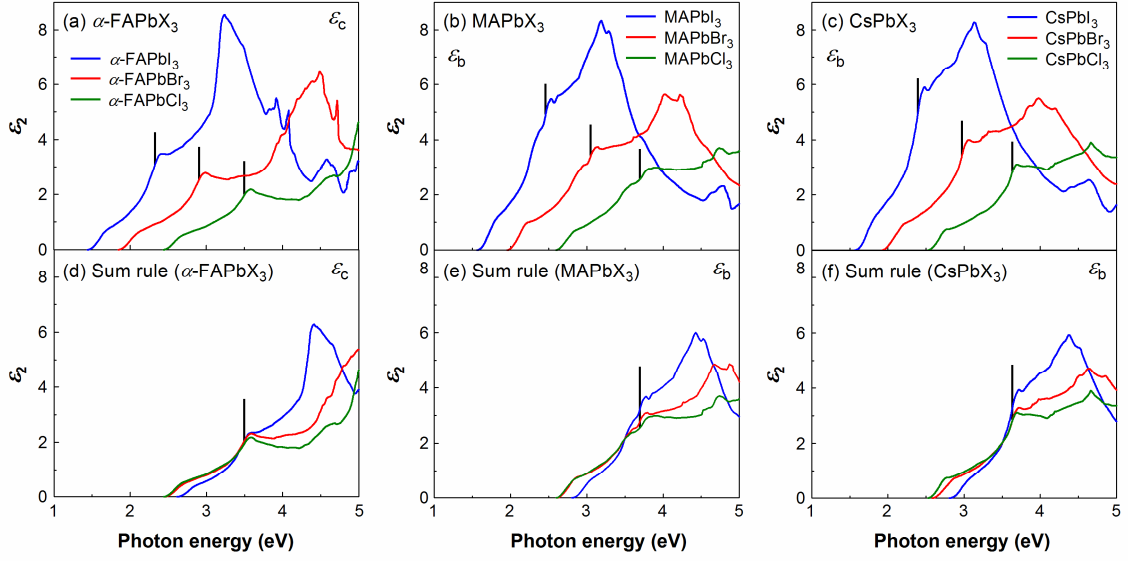


FIG. 12. ϵ_2 spectra of (a) α -FAPbX₃, (b) MAPbX₃, and (c) CsPbX₃ (X = I, Br, Cl) calculated from the DFT, together with the corresponding ϵ_2 spectra of (d) α -FAPbX₃, (e) MAPbX₃, and (f) CsPbX₃ obtained by applying the sum rule for APbI₃ and APbBr₃. In the figure, only the ϵ_2 spectra for ϵ_c (α -FAPbX₃) and ϵ_b (MAPbX₃ and CsPbX₃) are shown. The bars indicate the energy positions of the E_1 transition at the M_2 point (V_1C_1). The dielectric functions of (a)-(c) have been obtained by replacing the A-site cation in the identical PbX₃⁻ structures determined from the structural optimization of MAPbX₃.

To express the variation of the ϵ_2 spectrum with the A-site cation, we extract the ϵ_2 value for the E_1 transition at the M_2 point: i.e., the ϵ_2 value indicated by the bar in Figs. 12(a)-(c), for example. In Fig. 13(a), the extracted ϵ_2 values of APbX₃ are summarized as a function of the valence charge ratio expressed by Q_X/Q_{Total} . Here, Q_X shows the valence charge of the X atom along the a , b , and c axes in a selected energy region ($Q_{1,a-c}$ in Fig. 11, for example), while Q_{Total} denotes the total charge of APbX₃ in the same energy region. Thus, Q_X/Q_{Total} represents the relative magnitude of each X-site valence charge (i.e., $Q_{X,a}$, $Q_{X,b}$ or $Q_{X,c}$). For the Q_X/Q_{Total} calculation, we select the energy ranges of $-0.6 \sim -0.4$ eV (APbI₃), $-0.7 \sim -0.5$ eV (APbBr₃) and $-0.8 \sim -0.6$ eV (APbCl₃) from VBM ($E = 0$ eV), which correspond to the E_1 transitions at the M_2 point. It should be noted that, when the PbX₃⁻ structures derived from MAPbX₃ are assumed, the energies of the E_1 and E_2 transitions in α -FAPbX₃ become almost identical since the lattice parameters are quite similar in MAPbX₃. In Fig. 13(a), the results for ϵ_a , ϵ_b and ϵ_c in each APbX₃ are plotted.

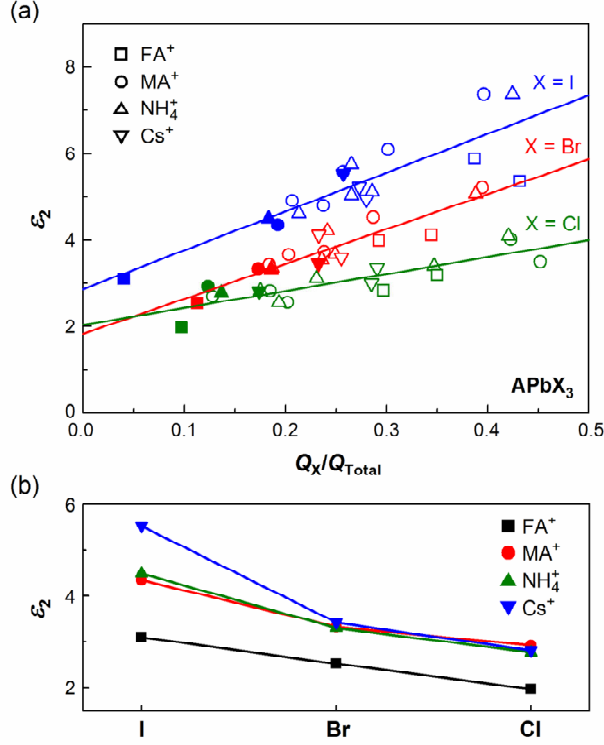


FIG. 13. (a) ϵ_2 values for the E_1 transition at the M_2 point (V_1C_1) in APbX_3 ($A = \text{FA}^+$, MA^+ , NH_4^+ , Cs^+ ; $X = \text{I}, \text{Br}, \text{Cl}$) as a function of the valence charge ratio expressed by Q_X/Q_{Total} and (b) ϵ_2 value for the lowest Q_X/Q_{Total} in each APbX_3 . The Q_X represents the valence charge of the X-site atom along the a , b , and c axes and is calculated by selecting an energy region that corresponds to the E_1 transition at the M_2 point (V_1C_1), whereas Q_{Total} denotes the total charge of APbX_3 in the same energy region. In (a), the closed symbol represents the plot for the lowest Q_X/Q_{Total} in each APbX_3 . In (b), the ϵ_2 values of the closed symbols in (a) are summarized.

For MAPbX_3 and NH_4PbX_3 in Fig. 13(a), the DFT calculations are also implemented by varying the N atom position within the PbX_3^- . Specifically, in this calculation, the N atom of MA^+ is shifted to the center position of the C–N bond in the optimized MAPbX_3 structure [see Fig. 11(c)]. In NH_4PbX_3 , the N atom position of NH_4^+ is quite similar to that of MA^+ ,⁵ and we also calculate the dielectric function of NH_4PbX_3 when NH_4^+ is placed at the center position of the unit cell.

In Fig. 13(a), the linear increase of ϵ_2 with Q_X/Q_{Total} is evident and the ϵ_2 value of ϵ_a , ϵ_b or ϵ_c in APbX_3 increases when the corresponding $Q_{X,a}$, $Q_{X,b}$ or $Q_{X,c}$ becomes larger.

The systematic variations of ε_2 with Q_X/Q_{Total} are represented quite well by the linear fitting results (solid lines), confirming the presence of a universal rule for the effect of the A-site cation. In Fig. 13(a), the slopes for the ε_2 change with Q_X/Q_{Total} are quite similar in APbI₃ and APbBr₃, while the ε_2 variation is suppressed in APbCl₃. The scatter of the plots reflects the fact that Q_X varies slightly by the X–Pb–X bond angle and bond length.

The closed symbol in Fig. 13(a) represents the ε_2 value for the lowest Q_X/Q_{Total} in each APbX₃ and these values are summarized in Fig. 13(b). Since the experimental optical properties are reproduced when the strong anti-coupling effect is considered, the ε_2 values of Fig. 13(b) approximate the light absorption strength in the hybrid perovskites. It is obvious that α -FAPbX₃ shows the lowest ε_2 , compared with the other APbX₃ perovskites. Because FA⁺ has two N atoms, a quite large anti-coupling interaction occurs in α -FAPbX₃, which in turn reduces the visible-light absorption significantly, as observed in Fig. 4. In contrast, Cs⁺ is stabilized at the center position of the PbX₃[−] cage and shows the weak anti-coupling effect. As a result, CsPbI₃ exhibits the highest ε_2 value among all the APbX₃ perovskites investigated here. This result is consistent with the observed increase in α by the incorporation of Cs into α -FAPbI₃.⁵³

We further find that the effect of X on the ε_2 spectrum can be expressed simply by the general sum rule:⁷⁰

$$\int E\varepsilon_2(E)dE = \text{const.} \quad (1)$$

As shown in Figs. 4 and 12(a)-(c), the replacement of X induces the spectrum shift and the whole ε_2 spectrum moves toward higher energy with decreasing halogen mass. This change can be reproduced quite well based on the sum rule. In particular, the sum rule requires that the ε_2 peak amplitude reduces to $E/(E + \Delta E)$ when the ε_2 spectrum is shifted toward higher energy by ΔE . In Figs. 12(d)-(f), the ε_2 spectra of APbI₃ and APbBr₃ are shifted so that the E_1 transition energies match that of APbCl₃. In this case, the amplitude of the shifted ε_2 spectra is reduced further by applying the sum rule. Under these assumptions, the ε_2 values for the E_1 transition become similar and all the spectra show reasonable overlap in the energy region of $E < 3.7$ eV. Accordingly, the ε_2 amplitude variation induced by X can simply be interpreted by the change in the transition energy. From Fig. 13(b), it can be seen that the ε_2 values reduce systematically with the order of I > Br > Cl, independent of the species of the A-site cation.

The above results indicate that the optical effects of the A-site cation and X-site halogen atom can be described separately according to the valence charge interaction and the sum rule, respectively. As a result, the optical interaction of the A-site cation in

APbX₃ perovskites can be categorized into two main factors: (i) slight E_g variation controlled primarily by the size of the A-site cation¹⁷ and (ii) large variation of α induced by the anti-coupling effect. In α -FAPbI₃, for example, E_g decreases slightly compared with MAPbI₃, but α decreases rather significantly by the strong anti-coupling effect. In contrast, the introduction of Cs⁺ increases α because of the weaker anti-coupling effect with a slight increase in E_g .

VI. DISCUSSION

In polycrystalline materials, optical anisotropy is generally not observed and the optical properties are expressed as the average response of each anisotropic component. In the case of the polycrystalline hybrid perovskites, therefore, the dielectric function corresponding to $(\epsilon_a + \epsilon_b + \epsilon_c)/3$ is expected to be observed experimentally. Rather surprisingly, the experimental ϵ_2 spectra of α -FAPbI₃, MAPbI₃ and MAPbBr₃ do not match those calculated assuming optical isotropy [i.e., $(\epsilon_a + \epsilon_b + \epsilon_c)/3$] and show excellent agreement with the DFT spectra obtained by maximizing the anti-coupling effect. In other words, the overall visible absorption in these perovskites is minimized by the strong anti-coupling interaction.

In our previous study for MAPbI₃,⁵ the large difference observed between the experimental and isotropic DFT [$(\epsilon_a + \epsilon_b + \epsilon_c)/3$] spectra was attributed to the rapid reorientation of the A-site cation. It is now well established that MA⁺ and FA⁺ in the PbI₃⁻ reorient rapidly with a time scale of 0.5–14 ps at room temperature.^{33-35,40-42,62} In the DFT calculation that assumes 0 K temperature, however, the cation position is fixed completely and the effect of the cation reorientation is neglected. Accordingly, the excellent agreement between the experimental and DFT results supports the fact that the N-I distance is close and the anti-coupling phenomenon persists even at room temperature even though the A-site cation reorients rapidly.

This puzzling result can be understood from the quite strong hydrogen-bonding interaction between the I and H–N. In particular, the molecular dynamics (MD) simulations of MAPbI₃ show that the orientation of the center cation is not completely random even at room temperature^{33-35,41,42,68,69} and the C–N axis of MA⁺ is preferentially directed toward the face center position of the cubic structure.^{33,41,42,68,69} In fact, the results obtained from the neutron scattering⁴¹ and ultrafast infrared-vibrational spectroscopy⁴² of MAPbI₃ are consistent with the MD simulation results, supporting the preferential orientations of MA⁺ within the PbI₃⁻ cage. The MD simulation of MAPbI₃

further reveals that the stable I-H distance of 2.65 Å is maintained at room temperature (268 K) due to the strong coupling of MA⁺ with PbI₃⁻.³⁴ Moreover, a recent large-scale MD simulation of MAPbI₃ shows that roughly half of MA⁺ are participating in hydrogen bonding.³⁵ The above results show that dynamical motion of MA⁺ is strongly correlated with the I atoms even at elevated temperatures due to the presence of I···H–N hydrogen bonding. Thus, if the close I-N distance is maintained statistically even during the continuous reorientation, the electrostatic anti-coupling interaction is still expected to occur.

A recent MD study further shows that the N-(C)-N axis of FA⁺ is directed toward the center of the cube face [see Fig. 8(a)], and FA⁺ rotates preferentially around the N-(C)-N axis.⁶² This simulation confirms quite intense hydrogen-bonding interaction in α -FAPbI₃ and suggests that the free motion of FA⁺ is hindered effectively by the I···H–N bonding that occurs at both ends of FA⁺. Accordingly, the significant anti-coupling effect observed in the room-temperature optical spectrum of α -FAPbI₃ can be interpreted by the strong hydrogen-bonding effect of FA⁺.

VII. CONCLUSION

To determine the optical effect of the A-site cation in APbI₃-type hybrid perovskites, the reliable optical constants of α -FAPbI₃ are determined without exposing the samples to humid air based on a self-consistent SE analysis. We find that the replacement of A = MA⁺ with FA⁺ reduces the overall amplitude of the ϵ_2 spectrum roughly by half and the resulting α values of α -FAPbI₃ become notably smaller than those of MAPbI₃. The CP analysis shows that E_g of α -FAPbI₃ is 1.55 ± 0.01 eV, and α -FAPbI₃ exhibits the sharp absorption edge with a low Urbach energy of 16 meV.

From the DFT calculations within the PBE without SOC, the optical transitions of α -FAPbI₃ and MAPbBr₃ are analyzed. Although the DFT-derived dielectric functions indicate highly anisotropic optical properties, the calculated dielectric functions show excellent agreement with the experimental spectra, reproducing all the fine-absorption features observed in α -FAPbI₃ and MAPbBr₃. For the assignment of the optical transitions, the dielectric response of each interband transition is calculated and the interband transitions at high symmetry points have been determined. The DFT calculation of the dielectric function further reveals that non-excitonic light absorption occurs in α -FAPbI₃.

Our analysis for the APbI₃ perovskites shows that the strong optical anisotropy

confirmed in the DFT results originates from the charge density distribution of the I-5*p* valence electron. In particular, the DFT calculation indicates that the formation of the hydrogen bonding between the I and H–N modifies the electronic state of the I atoms significantly and the valence charge density of the I atom reduces when the I-N distance is smaller. This anti-coupling effect is found to govern the visible light absorption and the transition probability reduces significantly when the anti-coupling interaction becomes stronger. Based on this finding, we establish a general rule that expresses the optical effect of the A-site cation ($A = \text{FA}^+, \text{MA}^+, \text{NH}_4^+, \text{Cs}^+$) within the PbX_3^- cage ($X = \text{I}, \text{Br}, \text{Cl}$). Since FA^+ has two N atoms, the anti-coupling interaction is maximized, lowering α values in $\alpha\text{-FAPbI}_3$, while CsPbI_3 shows the highest α due to the weak anti-coupling effect of Cs^+ . The systematic DFT calculations further show that the variation of the APbX_3 dielectric function with X can be approximated by the sum rule. From the above results, we propose universal rules that describe the effects of A and X on the visible light absorption separately. Our results demonstrate that experimental dielectric functions of various organic-inorganic hybrid perovskites can be predicted based on the polarization-dependent DFT calculations.

REFERENCES

- ¹M. Liu, M. B. Johnston, and H. J. Snaith, *Nature* **501**, 395 (2013).
- ²J. H. Heo, S. H. Im, J. H. Noh, T. N. Mandal, C.-S. Lim, J. A. Chang, Y. H. Lee, H.-J. Kim, A. Sarkar, M. K. Nazeeruddin, M. Grätzel, and S. I. Seok, *Nat. Photon.* **7**, 486 (2013).
- ³C. C. Stoumpos, C. D. Malliakas, and M. G. Kanatzidis, *Inorg. Chem.* **52**, 9019 (2013).
- ⁴B. Conings, J. Drijkoningen, N. Gauquelin, A. Babayigit, J. D'Haen, L. D'Olieslaeger, A. Ethirajan, J. Verbeeck, J. Manca, E. Mosconi, F. De Angelis, and H.-G. Boyen, *Adv. Energy Mater.* **5**, 1500477 (2015).
- ⁵M. Shirayama, H. Kadowaki, T. Miyadera, T. Sugita, M. Tamakoshi, M. Kato, T. Fujiseki, D. Murata, S. Hara, T. N. Murakami, S. Fujimoto, M. Chikamatsu, and H. Fujiwara, *Phys. Rev. Applied* **5**, 014012 (2016).
- ⁶G. Niu, X. Guo, and L. Wang, *J. Mater. Chem. A* **3**, 8970 (2015).
- ⁷T. Leijtens, G. E. Eperon, N. K. Noel, S. N. Habisreutinger, A. Petrozza, and H. J. Snaith, *Adv. Energy Mater.* **5**, 1500963 (2015).
- ⁸T. A. Berhe, W.-N. Su, C.-H. Chen, C.-J. Pan, J.-H. Cheng, H.-M. Chen, M.-C. Tsai, L.-Y. Chen, A. A. Dubale, and B.-J. Hwang, *Energy Environ. Sci.* **9**, 323 (2016).
- ⁹G. Murugadoss, S. Tanaka, G. Mizuta, S. Kanaya, H. Nishino, T. Umeyama, H. Imahori, and S. Ito, *Jpn. J. Appl. Phys.* **54**, 08KF08 (2015).
- ¹⁰J. H. Noh, S. H. Im, J. H. Heo, T. N. Mandal, and S. I. Seok, *Nano Lett.* **13**, 1764 (2013).
- ¹¹M. Shirayama, M. Kato, T. Miyadera, T. Sugita, T. Fujiseki, S. Hara, H. Kadowaki, D. Murata, M. Chikamatsu, and H. Fujiwara, *J. Appl. Phys.* **119**, 115501 (2016).
- ¹²T. Umebayashi, K. Asai, T. Kondo, and A. Nakao, *Phys. Rev. B* **67**, 155405 (2003).
- ¹³A. Filippetti, and A. Mattoni, *Phys. Rev. B* **89**, 125203 (2014).
- ¹⁴P. Umari, E. Mosconi, and F. De Angelis, *Sci. Rep.* **4**, 4467 (2014).
- ¹⁵F. Brivio, K. T. Butler, and A. Walsh, *Phys. Rev. B* **89**, 155204 (2014).
- ¹⁶E. Menéndez-Proupin, P. Palacios, P. Wahnón, and J. C. Conesa, *Phys. Rev. B* **90**, 045207 (2014).
- ¹⁷M. R. Filip, G. E. Eperon, H. J. Snaith, and F. Giustino, *Nat. Commun.* **5**, 5757 (2014).
- ¹⁸W.-J. Yin, J.-H. Yang, J. Kang, Y. Yan, and S.-H. Wei, *J. Mater. Chem. A* **3**, 8926 (2015).
- ¹⁹T. M. Brenner, D. A. Egger, L. Kronik, G. Hodes, and D. Cahen, *Nat. Rev. Mater.* **1**, 15007 (2016).

- ²⁰A. Amat, E. Mosconi, E. Ronca, C. Quarti, P. Umari, M. K. Nazeeruddin, M. Grätzel, and F. De Angelis, *Nano Lett.* **14**, 3608 (2014).
- ²¹G. Xing, N. Mathews, S. Sun, S. S. Lim, Y. M. Lam, M. Grätzel, S. Mhaisalkar, and T. C. Sum, *Science* **342**, 344 (2013).
- ²²M. A. Green, A. Ho-Baillie, and H. J. Snaith, *Nat. Photon.* **8**, 506 (2014).
- ²³Q. Lin, A. Armin, R. C. R. Nagiri, P. L. Burn, and P. Meredith, *Nat. Photon.* **9**, 106 (2015).
- ²⁴P. Löper, M. Stuckelberger, B. Niesen, J. Werner, M. Filipič, S.-J. Moon, J.-H. Yum, M. Topič, S. De Wolf, and C. Ballif, *J. Phys. Chem. Lett.* **6**, 66 (2015).
- ²⁵J. M. Ball, S. D. Stranks, M. T. Hörantner, S. Hüttner, W. Zhang, E. J. W. Crossland, I. Ramirez, M. Riede, M. B. Johnston, R. H. Friend, and H. J. Snaith, *Energy Environ. Sci.* **8**, 602 (2015).
- ²⁶Y. Jiang, M. A. Green, R. Sheng, and A. Ho-Baillie, *Sol. Eng. Mater. Sol. Cells* **137**, 253 (2015).
- ²⁷A. M. A. Leguy, P. Azarhoosh, M. I. Alonso, M. Campoy-Quiles, O. J. Weber, J. Yao, D. Bryant, M. T. Weller, J. Nelson, A. Walsh, M. van Schilfgaarde, and P. R. F. Barnes, *Nanoscale* **8**, 6317 (2016).
- ²⁸S. De Wolf, J. Holovsky, S.-J. Moon, P. Löper, B. Niesen, M. Ledinsky, F.-J. Haug, J.-H. Yum, and C. Ballif, *J. Phys. Chem. Lett.* **5**, 1035 (2014).
- ²⁹E. Mosconi, A. Amat, M. K. Nazeeruddin, M. Grätzel, and F. De Angelis, *J. Phys. Chem. C* **117**, 13902 (2013).
- ³⁰J. Even, L. Pedesseau, J.-M. Jancu, and C. Katan, *J. Phys. Chem. Lett.* **4**, 2999 (2013).
- ³¹C. Quarti, E. Mosconi, and F. De Angelis, *Chem. Mater.* **26**, 6557 (2014).
- ³²C. Motta, F. El-Mellouhi, S. Kais, N. Tabet, F. Alharbi, and S. Sanvito, *Nat. Commun.* **6**, 7026 (2015).
- ³³A. Mattoni, A. Filippetti, M. I. Saba, and P. Delugas, *J. Phys. Chem. C* **119**, 17421 (2015).
- ³⁴E. Mosconi, C. Quarti, T. Ivanovska, G. Ruani, and F. De Angelis, *Phys. Chem. Chem. Phys.* **16**, 16137 (2014).
- ³⁵M. A. Carignano, and A. Kachmar, *J. Phys. Chem. C* **119**, 8991 (2015).
- ³⁶J.-H. Lee, N. C. Bristowe, P. D. Bristowe, and A. K. Cheetham, *Chem. Commun.* **51**, 6434 (2015).
- ³⁷J. H. Lee, J.-H. Lee, E.-H. Kong, and H. M. Jang, *Sci. Rep.* **6**, 21687 (2016).
- ³⁸J. S. Bechtel, R. Seshadri, and A. Van der Ven, *J. Phys. Chem. C* **120**, 12403 (2016).
- ³⁹J. H. Lee, N. C. Bristowe, J. H. Lee, S. H. Lee, P. D. Bristowe, A. K. Cheetham, and H. M. Jang, *Chem. Mater.* **28**, 4259 (2016).

- ⁴⁰R. E. Wasylshen, O. Knop, and J. B. Macdonald, *Solid State Commun.* **56**, 581 (1985).
- ⁴¹A. M. A. Leguy, J. M. Frost, A. P. McMahon, V. G. Sakai, W. Kochelmann, C. Law, X. Li, F. Foglia, A. Walsh, B. C. O'Regan, J. Nelson, J. T. Cabral, and R. F. Barnes, *Nat. Commun.* **6**, 7124 (2015).
- ⁴²A. A. Bakulin, O. Selig, H. J. Bakker, Y. L. A. Rezus, C. Müller, T. Glaser, R. Lovrincic, Z. Sun, Z. Chen, A. Walsh, J. M. Frost, and T. L. C. Jansen, *J. Phys. Chem. Lett.* **6**, 3663 (2015).
- ⁴³A. M. A. Leguy, Y. Hu, M. Campoy-Quiles, M. I. Alonso, O. J. Weber, P. Azarhoosh, M. van Schilfgaarde, M. T. Weller, T. Bein, J. Nelson, P. Docampo, and P. R. F. Barnes, *Chem. Mater.* **27**, 3397 (2015).
- ⁴⁴J. Kim, S.-C. Lee, S.-H. Lee, and K.-H. Hong, *J. Phys. Chem. C* **119**, 4627 (2015).
- ⁴⁵T. M. Koh, K. Fu, Y. Fang, S. Chen, T. C. Sum, N. Mathews, S. G. Mhaisalkar, P. P. Boix, and T. Baikie, *J. Phys. Chem. C* **118**, 16458 (2014).
- ⁴⁶G. E. Eperon, S. D. Stranks, C. Menelaou, M. B. Johnston, L. M. Herz, and H. J. Snaith, *Energy Environ. Sci.* **7**, 982 (2014).
- ⁴⁷S. Pang, H. Hu, J. Zhang, S. Lv, Y. Yu, F. Wei, T. Qin, H. Xu, Z. Liu, and G. Cui, *Chem. Mater.* **26**, 1485 (2014).
- ⁴⁸A. Binek, F. C. Hanusch, P. Docampo, and T. Bein, *J. Phys. Chem. Lett.* **6**, 1249 (2015).
- ⁴⁹Q. Han, S.-H. Bae, P. Sun, Y.-T. Hsieh, Y. Yang, Y. S. Rim, H. Zhao, Q. Chen, W. Shi, G. Li, and Y. Yang, *Adv. Mater.* **28**, 2253 (2016).
- ⁵⁰M. T. Weller, O. J. Weber, J. M. Frost, and A. Walsh, *J. Phys. Chem. Lett.* **6**, 3209 (2015).
- ⁵¹N. Pellet, P. Gao, G. Gregori, T.-Y. Yang, M. K. Nazeeruddin, J. Maier, and M. Grätzel, *Angew. Chem. Int. Ed.* **53**, 3151 (2014).
- ⁵²W. S. Yang, J. H. Noh, N. J. Jeon, Y. C. Kim, S. Ryu, J. Seo, and S. I. Seok, *Science* **348**, 1234 (2015).
- ⁵³J.-W. Lee, D.-H. Kim, H.-S. Kim, S.-W. Seo, S. M. Cho, and N.-G. Park, *Adv. Energy Mater.* **5**, 1501310 (2015).
- ⁵⁴Z. Li, M. Yang, J.-S. Park, S.-H. Wei, J. J. Berry, and K. Zhu, *Chem. Mater.* **28**, 284 (2016).
- ⁵⁵C. Yi, J. Luo, S. Meloni, A. Boziki, N. Ashari-Astani, C. Grätzel, S. M. Zakeeruddin, U. Röthlisberger, and M. Grätzel, *Energy Environ. Sci.* **9**, 656 (2016).
- ⁵⁶D. P. McMeekin, G. Sadoughi, W. Rehman, G. E. Eperon, M. Saliba, M. T. Hörantner, A. Haghighirad, N. Sakai, L. Korte, B. Rech, M. B. Johnston, L. M. Herz, and H. J.

- Snaith, *Science* **351**, 151 (2016).
- ⁵⁷M. Saliba, T. Matsui, J.-Y. Seo, K. Domanski, J.-P. Correa-Baena, M. K. Nazeeruddin, S. M. Zakeeruddin, W. Tress, A. Abate, A. Hagfeldt, and M. Grätzel, *Energy Environ. Sci.* doi: 10.1039/c5ee03874j (2016).
- ⁵⁸D. Bi, W. Tress, M. I. Dar, P. Gao, J. Luo, C. Renevier, K. Schenk, A. Abate, F. Giordano, J.-P. Correa Baena, J.-D. Decoppet, S. M. Zakeeruddin, M. K. Nazeeruddin, M. Grätzel, and A. Hagfeldt, *Sci. Adv.* **2**, e1501170 (2016).
- ⁵⁹T. J. Jacobsson, J.-P. Correa-Baena, M. Pazoki, M. Saliba, K. Schenk, M. Grätzel, and A. Hagfeldt, *Energy Environ. Sci.* doi: 10.1039/c6ee00030d (2016).
- ⁶⁰J.-W. Lee, D.-J. Seol, A.-N. Cho, and N.-G. Park, *Adv. Mater.* **26**, 4991 (2014).
- ⁶¹P. F. Ndione, Z. Li, and K. Zhu, *J. Mater. Chem. C* **4**, 7775 (2016).
- ⁶²M. A. Carignano, Y. Saeed, S. A. Aravindh, I. S. Roqan, J. Even, and C. Katan, *Phys. Chem. Chem. Phys.* **18**, 27109 (2016).
- ⁶³J.-S. Park, S. Choi, Y. Yan, Y. Yang, J. M. Luther, S.-H. Wei, P. Parilla, and K. Zhu, *J. Phys. Chem. Lett.* **6**, 4304 (2015).
- ⁶⁴C. Motta, F. El-Mellouhi, and S. Sanvito, *Phys. Rev. B* **93**, 235412 (2016).
- ⁶⁵D. Li, J. Meng, Y. Niu, H. Zhao, and C. Liang, *Chem. Phys. Lett.* **627**, 13 (2015).
- ⁶⁶J. Brgoch, A. J. Lehner, M. Chabynyc, and R. Seshadri, *J. Phys. Chem. C* **118**, 27721 (2014).
- ⁶⁷G. R. Berdiyrov, A. Kachmar, F. El-mellouhi, M. A. Carignano, and M. E. A. Madjet, *J. Phys. Chem. C* **120**, 16259 (2016).
- ⁶⁸J. Even, M. Carignano, and C. Katan, *Nanoscale* **8**, 6222 (2016).
- ⁶⁹I. Deretzis, B. N. D. Mauro, A. Alberti, G. Pellegrino, E. Smecca, and A. L. Magna, *Scientific reports*, **6**, 24443 (2016).
- ⁷⁰M. P. Marder, *Condensed Matter Physics* (Wiley, Hoboken, 2010).
- ⁷¹H. Fujiwara, *Spectroscopic Ellipsometry: Principles and Applications* (Wiley, West Sussex, 2007).
- ⁷²H. Fujiwara, J. Koh, P. I. Rovira, and R. W. Collins, *Phys. Rev. B* **61**, 10832 (2000).
- ⁷³J. P. Perdew, K. Burke, and M. Ernzerhof, *Phys. Rev. Lett.* **77**, 3865 (1996).
- ⁷⁴H. Kageshima, and K. Shiraishi, *Phys. Rev. B* **56**, 14985 (1997).
- ⁷⁵N. Kitazawa, Y. Watanabe, and Y. Nakamura, *J. Mater. Sci.* **37**, 3585 (2002).
- ⁷⁶S. Adachi, *The Handbook on Optical Constants of Metals: In Tables and Figures* (World Scientific, Singapore, 2012).
- ⁷⁷J.-H. Kwon, S.-I. Shin, J. Choi, M.-H. Chung, T.-Y. Oh, K.-H. Kim, M. J. Cho, K. N. Kim, D. H. Choi, and B.-K. Ju, *Organic Electronics* **10**, 729 (2009).
- ⁷⁸T. Hara, T. Maekawa, S. Minoura, Y. Sago, S. Niki, and H. Fujiwara, *Phys. Rev.*

- Applied **2**, 034012 (2014).
- ⁷⁹O. N. Yunakova, V. K. Miloslavskii, and E. N. Kovalenko, *Opt. Spectrosc.* **112**, 91 (2012).
- ⁸⁰F. Hao, C. C. Stoumpos, Z. Liu, R. P. H. Chang, and M. G. Kanatzidis, *J. Am. Chem. Soc.* **136**, 16411 (2014).
- ⁸¹G. E. Jellison Jr., and F. A. Modine, *Appl. Phys. Lett.* **69**, 371 (1996); Erratum, *Appl. Phys. Lett.* **69**, 2137 (1996).
- ⁸²R. W. Godby, M. Schlüter, and L. J. Sham, *Phys. Rev. B* **37**, 10159 (1988).
- ⁸³G. E. Eperon, G. M. Paternò, R. J. Sutton, A. Zampetti, A. A. Haghighirad, F. Cacialli, and H. J. Snaith, *J. Mater. Chem. A* **3**, 19688 (2015).
- ⁸⁴T. S. Ripolles, K. Nishinaka, Y. Ogomi, Y. Miyata, and S. Hayase, *Sol. Energy Mater. Sol. Cells* **114**, 532 (2016).